

1 **Post-failure evolution analysis of a rainfall-triggered landslide**
2 **by Multi-Temporal Interferometry SAR approaches**
3 **integrated with geotechnical analysis**

4

5 **Pierluigi Confuorto** - Department of Earth Sciences, Environment and Resources, Federico II University of
6 Naples, Largo San Marcellino 10, 80138 Naples, Italy. E-mail: pierluigi.confuorto@unina.it

7 **Diego Di Martire** - Department of Earth Sciences, Environment and Resources, Federico II University of
8 Naples, Largo San Marcellino 10, 80138 Naples, Italy. E-mail: diego.dimartire@unina.it

9 **Giuseppe Centolanza** - Remote Sensing Laboratory (RSLab), Department of Signal Theory and
10 Communications, Universitat Politècnica de Catalunya, c/Jordi Girona 1-3, Ed. D-3, 08304 Barcelona, Spain.
11 E-mail: giuseppe.centolanza@tsc.upc.edu

12 **Ruben Iglesias** - Remote Sensing Laboratory (RSLab), Department of Signal Theory and Communications,
13 Universitat Politècnica de Catalunya, c/Jordi Girona 1-3, Ed. D-3, 08304 Barcelona, Spain. E-mail:
14 ruben.iglesias@tsc.upc.edu

15 **Jordi J. Mallorqui** - Remote Sensing Laboratory (RSLab), Department of Signal Theory and
16 Communications, Universitat Politècnica de Catalunya, c/Jordi Girona 1-3, Ed. D-3, 08304 Barcelona, Spain.
17 E-mail: mallorqui@tsc.upc.edu

18 **Alessandro Novellino** - Geomatic Ventures Ltd, Nottingham, UK, c/o University Of Nottingham,
19 Nottingham Geospatial Building, Triumph Road, Nottingham, East Midlands, UK; E-Mail:
20 alessandro.novellino@geomaticventures.com

21 **Simon Plank** - German Aerospace Center (DLR), German Remote Sensing Data Center (DFD),
22 Oberpfaffenhofen, Münchener Straße 20, 82234 Weßling (Germany) simon.plank@dlr.de

23 **Massimo Ramondini** - Department of Civil, Architectural and Environmental Engineering, Federico II

24 University of Naples, via Claudio 21, 80125 Naples, Italy. E-mail: ramondin@unina.it

25 **Kuroschi Thuro** - Chair for Engineering Geology, Technische Universität München (TUM); Arcistraße 2,

26 80333 Munich (Germany) E-mail : thuro@tum.de

27 **Domenico Calcaterra** - Department of Earth Sciences, Environment and Resources, Federico II University of Naples,

28 Largo San Marcellino 10, 80138 Naples, Italy. E-mail: domenico.calcaterra@unina.it

29 **Author to whom correspondence should be addressed; emails: diego.dimartire@unina.it; Tel.: +39-**

30 **081-2538117; Largo San Marcellino, 10, 80138 Naples, Italy**

31

32 **Abstract**

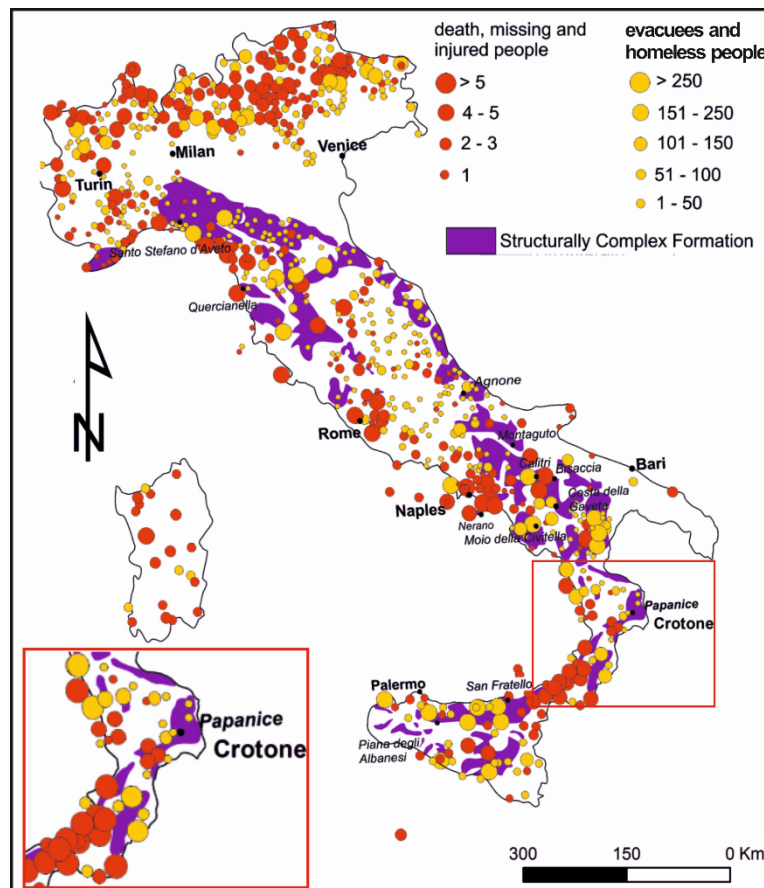
33 Persistent Scatterers Interferometry (PSI) represents one of the most powerful techniques for Earth's surface
34 deformation processes' monitoring, especially for long-term evolution phenomena. In this work, a dataset of 34
35 TerraSAR-X StripMap images (October 2013-October 2014) has been processed by two PSI techniques - Coherent
36 Pixel Technique-Temporal Sublook Coherence (CPT-TSC) and Small Baseline Subset (SBAS) - in order to study the
37 evolution of a slow-moving landslide which occurred on February 23, 2012 in the Papanice hamlet (Crotona
38 municipality, southern Italy) and induced by a significant rainfall event (185 mm in three days). The mass movement
39 caused structural damage (buildings' collapse), and destruction of utility lines (gas, water and electricity) and roads.
40 The results showed analogous displacement rates (30-40 mm/yr along the Line of Sight –LOS - of the satellite) with
41 respect to the pre-failure phase (2008-2010) analyzed in previous works. Both approaches allowed to detect the
42 landslide-affected area, however the higher density of targets identified by means of CPT-TSC enabled to analyze in
43 detail the slope behavior in order to design possible mitigation interventions. For this aim, a slope stability analysis has
44 been carried out, considering the comparison between groundwater oscillations and time-series of displacement.
45 Hence, the crucial role of the interaction between rainfall and groundwater level has been inferred for the landslide
46 triggering. In conclusion, we showed that the integration of geotechnical and remote sensing approaches can be seen
47 as a best practice to support stakeholders to design remedial works.

48 **Keywords:** Persistent Scatterers Interferometry; SAR; Coherent Pixels Technique-Temporal Sublook Coherence;
49 Small Baseline Subset; Landslide; Crotona Province; Slope stability analysis.

50

51 **1. Introduction**

52 Ground failures and ground instability hazards are globally widespread phenomena caused by natural geological
53 and climatic processes such as landslides and slope movements (Di Martire et al., 2016a), soil volumetric changes in
54 relation to dry and wet periods, soil/rock dissolution, oscillations of groundwater levels (Chaussard et al., 2014), seismic
55 and volcanic activity (Lagios et al., 2013), neo-tectonic uplift or subsidence (Di Martire et al., 2016b) or induced by
56 anthropogenic sources such as ground water pumping, (Modoni et al., 2013), inappropriate water management
57 (Valipour et al., 2015 and references therein), gas and oil withdrawal, mining activity (Ferretti et al., 2011b), subsurface
58 and surface engineering works (Bandini et al., 2015). They determine a significant number of human losses and injury
59 as well as extensive economic damage to private and public properties. (Schuster & Fleming, 1986). In Europe and
60 especially in Italy, slope instabilities represent the primary cause of death caused by natural hazards (Guzzetti et al.,
61 2012). A recent statement by the Research Institute for Geo-Hydrological Protection (IRPI) (Figure 1), affirms that in
62 Italy landslides are “recurrent, widespread and dangerous phenomena” and in the first semester of the 2015 only, 3
63 victims and 9 casualties have been already reported (IRPI, 2015). The landslide risk scenario has worsened in the last 50
64 years, in relation with an inappropriate land management, following the “economic miracle” of the early 60s, which
65 increased the exposure to natural hazards for Italian towns (Di Martire et al., 2012). Most of the Southern Italy
66 landslides classified as slow to moderate kinematic (Cruden & Varnes, 1996) are rainfall-triggered: significant
67 examples are represented by the cases of Agnone (200 mm in the 72 hours before the event) (Calcaterra et al., 2008),
68 Maierato (200 mm in 15 days) (Gattinoni et al., 2012) San Fratello (900 mm in 4 months) (Bardi et al., 2014; Bianchini
69 et al., 2015) and Montescaglioso (246 mm in 72 hours) (Manconi et al., 2014). These events are comparable in terms of
70 geological and geomorphological settings as well as of poor geotechnical properties of the involved materials. The latter
71 correspond to clay-dominant tectonized terrains, geologically and geotechnically known as Structurally Complex
72 Formations (SCF) (Esu, 1977). The adverb “complex” refers to heterogeneity with respect to the epigenetic lithological
73 characteristics, while “structurally” points to the effect of tectonic processes due to syngenetic folding, faulting or
74 fracturing. Such a complexity poses major difficulties in terms of obtaining and testing representative samples to be
75 used to formulate suitable models for slope stability in order to plan mitigation works.



76

77 **Figure 1** - Map of the landslide events with “victims” in the time span 1964-2013, with the spread of the Structurally
 78 Complex Formations (SCFs) in the whole Italian territory (modified from IRPI, 2015). In the red box, Calabria region.

79 Globally slope movements in SCFs and in weak soils have a long evolutionary history characterized by several
 80 reactivations of the previously deformed mass in case of prolonged or intense rainfalls, seismic events or human
 81 activities (D’Elia et al., 1998; Bozzano et al., 2004; Di Maio et al., 2010). For this reason, the monitoring phase
 82 represents a paramount task for geoscientists and for public administrations to reduce or avoid potential calamities. In
 83 the last decades, remote sensing devices provided an important support in landslide monitoring at relatively low costs
 84 (Tofani et al., 2013; Scaioni et al., 2014). Among the remote sensing techniques (GPSs, Laser scanners, LiDAR, etc.),
 85 Persistent Scatterers Interferometry (PSI, Hooper et al., 2004), which represents an advanced configuration of classical
 86 Synthetic Aperture Radar Differential Interferometry (DInSAR), is surely one of the most valuable tools which has
 87 achieved relevant improvements within the last two decades (Colesanti & Wasowski, 2006; Cascini et al., 2010; Calò et
 88 al., 2012; Herrera et al., 2013; Novellino et al., 2015; Boni et al., 2016), in particular thanks to Very High Resolution
 89 images (VHR) (StripMap, up to 3 m resolution; SpotLight, up to 1 m resolution) and short revisit time of the latest
 90 space-born constellations (6-11 days - TerraSAR-X, COSMO-SkyMed and SENTINEL-1A and 1B).

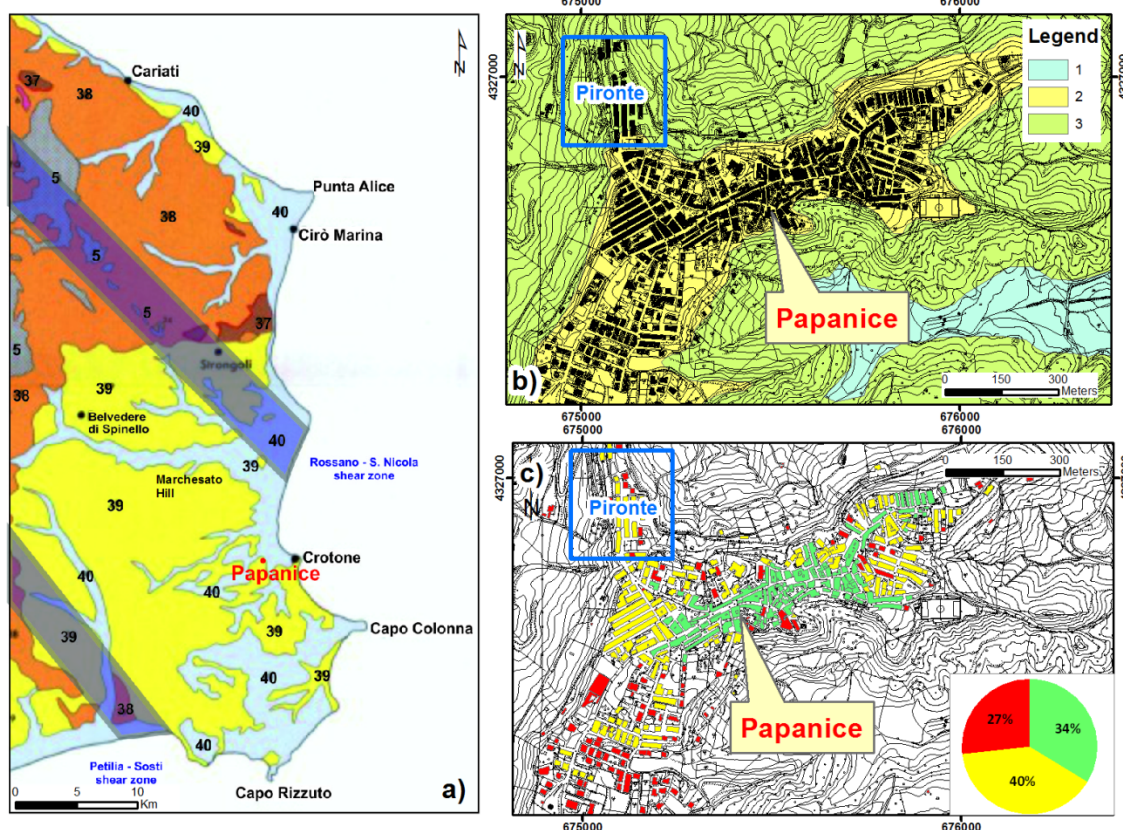
91 Many PSI techniques have been developed in the last 15 years (e.g., Permanent Scatterer - PS (Ferretti et al.,
92 2001), Small Baseline Subset Approach – SBAS (Berardino et al., 2002), SqueeSAR (Ferretti et al., 2011) and
93 Coherence Pixel Technique – CPT (Mora et al., 2003; Blanco-Sanchez et al., 2008; Iglesias et al., 2014a), allowing to
94 capitalize large SAR datasets and hence to investigate long-term events with the generation of precise time series of
95 ground-displacements. In this work, two PSI techniques have been applied: SBAS, implemented on the SARscape
96 software (www.sarmap.ch), and CPT, developed on the SUBSOFT processor (Mora et al., 2003). Such approaches have
97 been selected and applied to Papanice, a hamlet in Crotona suburb (Southern Italy), in order to analyze the post-failure
98 evolution of the landslide occurred in February 2012, and to integrate the previous analysis concerning the pre-failure
99 phase (Confuorto et al., 2015). The pre-failure analysis (2008-2010) showed how both PSI approaches were able to
100 identify displacement rates up to 30 mm/yr along the Line of Sight (LOS) direction. For this work, the dataset consists
101 of 34 TerraSAR-X images, acquired over ascending pass (October 2013 – October 2014). The novelty of this work is
102 represented by the detailed analysis of a landslide for different stages of its state of activity, because of the high spatial
103 and temporal resolutions of the multiple monitoring techniques available. The integration of different monitoring
104 systems can assume a key role in planning of remedial works, in order to assure the stability of urban settings. This has
105 allowed to evaluate the hydrologic mechanism that control the landslide dynamic and, ultimately, the landscape
106 evolution and hazard assessment within the study area, a finding that in previous earthflows studies (Bardi et al., 2014;
107 Raspini et al., 2015), especially for southern Apennines, is usually associated with considerable uncertainty. Moreover,
108 the application of PSI techniques has been for the first time tested for landslide studies in Crotona province, after
109 Confuorto et al., (2014, 2015).

110 The paper is organized as follows: first, the Papanice test site is described and a brief depiction of the rainfall
111 event which triggered the landslide is reported. The Papanice landslide is successively described according to field and
112 monitoring survey. Further, an overview of basic concepts of PSI technique is given also showing the deformation rates
113 obtained by combining CPT and SBAS processing. At the end, SAR results are integrated with geotechnical analyses,
114 such as the slope stability test, showing the important role of rainfall and of groundwater level as well for the trigger of
115 landslides in such contexts.

116 **2. Geological and Geomorphological Setting**

117 Papanice is a small settlement of ca. 3500 people, 11 km east from Crotona city center, on the top of the NW-SE
118 trending Marchesato hill (Figure 2a). Papanice is included in the Crotona Basin, a large sedimentary basin, whose
119 opening began between the Middle and the Upper Miocene (Serravallian and Tortonian) (Roda, 1964; Van Dijk, 1990).
120 The Crotona Basin is bounded by two main shear-zones: the Rossano-San Nicola shear zone in the northern sector, and

121 the Petilia-Sosti one in the southern part (Meulenkamp et al., 1986; Van Dijk & Okkes, 1990, 1991; Van Dijk, 1991)
122 (Figure 2a). In detail, the Papanice bedrock belongs to the most recent part of the Crotona Basin, where the Cutro
123 marly-clayey formation crops out. Locally such formation can reach a thickness of few hundred meters and it is
124 essentially made of marly and silty clay strata (Massari et al., 2002; Zecchin et al., 2012). The so-called S. Anna
125 Synthem, in form of marine terraces, overlies the Cutro marly-clayey formation and represents the unit where the
126 Papanice settlement arises. The synthem is composed of sands and conglomerates, at time intercalated with bioclastic
127 limestones (Figure 2b). No evidence of tectonic deformations have been recognized in the study area, where the weak
128 resistance to the erosion and the low permeability of the Cutro marly-clayey formation and Sant'Anna Synthem, make
129 the Papanice succession very prone to instability phenomena. The area of the 2012 Papanice landslides, the Pironte
130 district, is, from a geomorphological point of view, a N-S oriented peninsula, whose upper surface is characterized by a
131 flat area or locally with weak gradient, while the surrounding slopes present a higher inclination. This kind of setting is
132 very prone to generate gravitational phenomena, especially during strong precipitation events as well as seasonal
133 streams. When the instabilities have a retrogressive evolution (WP/WLI, 1993) they involve the buildings located at the
134 edge of the Pironte area. As shown in the Landslide Inventory Map of the Hydro-Geomorphological Setting Plan (HSP)
135 (Calabria Regional Basin Authority, 2006), the whole settlement is surrounded by landslides (Figure 3): most of them
136 can be classified as areas affected by deep slow deformation, but slide and complex phenomena also occur (Cruden &
137 Varnes, 1996). In the detail, the Pironte neighborhood is affected by two different dormant landslides, on the slope
138 facing east: an area affected by deep slow deformation and a rotational slide. The geomorphological setting of the area
139 has been severely modified by the intense growth of Papanice, started in the early 60s: indeed, 50 years ago the Pironte
140 area was almost uninhabited (Figure 2c). Only 30% of the whole urban area is dated before 1955, while the major
141 development started in 1956, and still in recent years (from 1983 onward) an evolution can be recorded, especially in
142 the NW sector, where the Pironte neighborhood is located, and in the SW sector of the settlement. This urban growth
143 also altered the risk scenario, exposing more areas to landslide hazard. In addition, the use of landfill materials to
144 reshape terrains by flattening areas has worsened the local geotechnical setting.



145

146 **Figure 2** - a) Geological sketch map of Crotona province: 5 – Meta-limestones, phyllites (Devonian age); 6 – Granites
 147 (Permian-Carboniferous age); 37 - Varicolored clays (Tortonian age); 38 - Clays and marls, evaporitic deposits (Lower
 148 Pliocene-Tortonian age); 39 – Calcarenes, sands, clays and conglomerates (Lower Pleistocene – Middle Pleistocene
 149 age); 40 – Alluvial deposits (Holocene – Upper Pleistocene). In blue bands, the two shear zones. Modified from
 150 Bonardi et al., 1976 ; b) Geological sketch map of Papanice area: 1 - Recent Alluvial Deposits (Holocene), 2 -
 151 Sant’Anna Synthem (Ionian), 3 - Cutro marly-clayey Formation (Piacentian – Calabrian) (SCF formation). In blue
 152 square, Pironte district; c) Urban evolution of Papanice settlement during 1953-2014: green = urban area before 1955,
 153 yellow= 1956-1982 expansion, red= 1983-2014 expansion (modified from ARPACAL, 2013). In blue square, Pironte
 154 district.

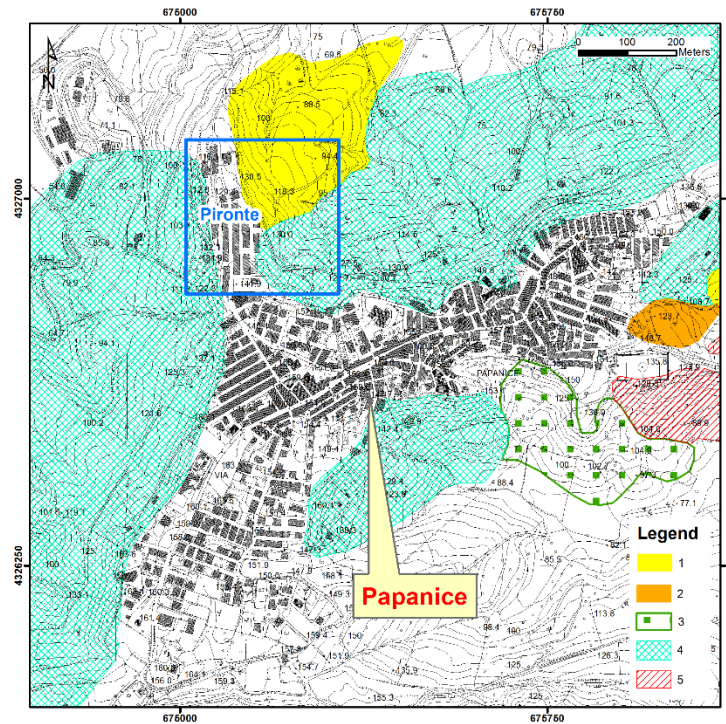
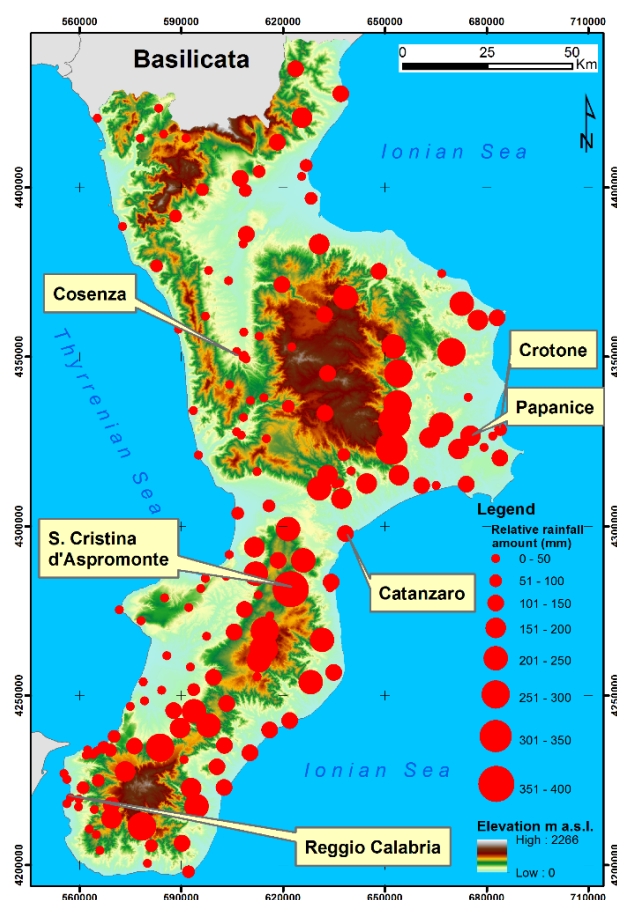


Figure 3 - Landslide inventory map of Papanice, modified from Calabria Regional Basin Authority, 2006. 1) Slide; 2) Complex landslide; 3) Area affected by shallow slow deformation/movements; 4) Area affected by deep slow deformation/movements; 5) Area affected by deep erosion. The blue square marks the area interested by the 2012 landslides (Pironte district).

3. Rainfall analysis

Precipitations play an important role in global energy, therefore their accurate knowledge assumes a major significance for land use management, agriculture hydrology and for landslide and flooding risk reduction (Schneider et al., 2011; Valipour, 2016). Between February 21 and February 23, 2012, an intense and prolonged rainfall event occurred in Calabria Region, with the most significant precipitations being registered on February 22. Starting from February 21, an intense cloudiness generated a high instability on the Ionian coastline of Calabria with frequent showers and thunderstorms. The precipitations became stronger, as shown by the daily value of 126.8 mm registered in the rain gauge of Santa Cristina d'Aspromonte at midnight February 21. On February 22, the precipitations on the Ionian sector of Calabria intensified: they first hit the SE Ionian Coast and then the Crotone area. On February 23, the phenomenon became less concentrated, characterized by a reduction of the rainfalls on the Ionian area, with still diffuse but less intense rain. The availability of a capillary network (252 rain gauges), set up by the Multi-hazard Functional Center of the Calabrian Regional Agency for the Environmental Protection (ARPACAL) covering the whole regional territory

173 (Figure 4), allowed to rebuild the spatial distribution of precipitations during these 3 days. In many areas along the
 174 Ionian coast and in the inner part of the region, the daily precipitations exceeded 200 mm. In the Papanice area, rainfall
 175 data have been collected from the Crotona – Papanice rain gauge (Figure 5a), located at a distance of 200 m from the
 176 landslide area, and plotted as cumulated rainfall for the year 2012 (640 mm; Figure 5b), February 2012 (280 mm;
 177 Figure 5c) and the 19-25 February weekly rainfalls (185 mm; Figures 5d). It is worth pointing out that the analysis of
 178 the precipitation occurring in the previous 15 years shows an increase in the three years preceding the main landslide
 179 event (2009-2011), recording in this case an annual average of 1001.7 mm (1,092.2 mm for 2009, 1,025.9 for 2010 and
 180 887.0 for 2011), while the average annual value of Papanice, recorded between 1998 and 2009, is of about 652 mm
 181 (Table 1), from a minimum of 375.0 mm in 2001 to a maximum of 862.8 in 2004. In this case, an increase of 35% has
 182 been reported in the three years preceding the 2012 landslide event, pointing out the role of precipitations for ground
 183 failure. However, such finding cannot be attributed to a general precipitation increase tendency. As reported in Brunetti
 184 et al. (2004), a negative trend in number of wet days is shown all over Italy, while a positive trend in precipitation
 185 intensity can be noted. Therefore, the increase of rainfall amount in the years preceding landslide event can be
 186 connected to more high intensity precipitation events

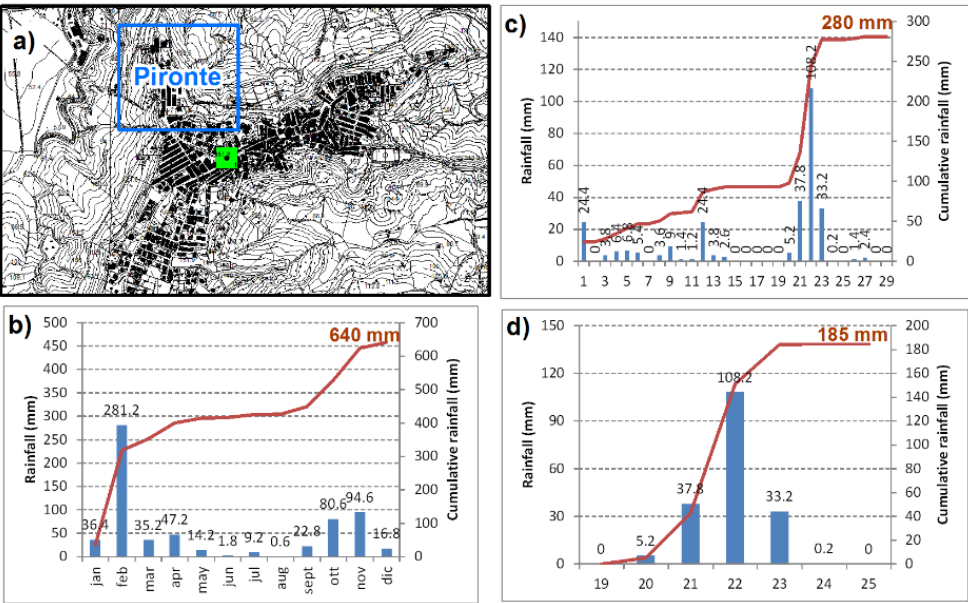


188 **Figure 4** - Localization of the measurement stations of the Multi-hazard Functional Center of the ARPACAL and
189 rainfall amount for the period 21-23 February 2012.

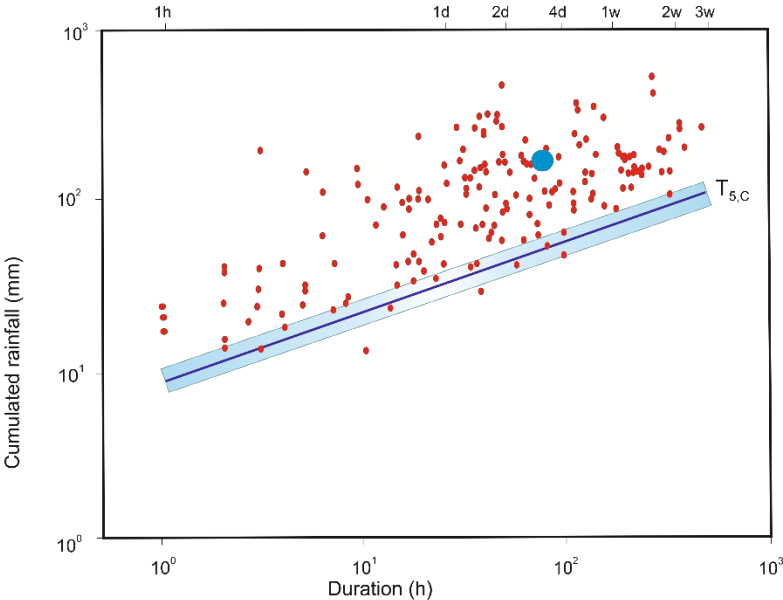
190 **Table 1** - Annual rainfall (mm) from 1998 to 2012 recorded at Papanice rain gauge.

Year	Rainfall (mm)
1998	419.6
1999	495.6
2000	505.4
2001	375.0
2002	740.2
2003	640.4
2004	862.8
2005	585.2
2006	558.6
2007	410.8
2008	536.9
2009	1,092.2
2010	1,025.9
2011	887.0
2012	640.0

191 To this regard, the February 2012 precipitations are equal to 45% (280 mm out of 640 mm) of the annual rainfall
192 occurred and the pre-event rainfall (21-23rd of February) corresponds to 28% of the 2012 annual amount (180 mm out
193 of 640 mm), hence representing the triggering factors for the reactivation of the landslide. Taking into account the work
194 of Vennari et al. (2014), which deals with the rainfall thresholds for shallow landslide occurrence in Calabria, the pre-
195 event rainfall has been plotted on the duration versus the cumulated rainfall graph (Figure 6). The Papanice case
196 conditions perfectly match the circumstances resulting in shallow landslides in Calabria.



198 **Figure 5.** a) Localization of Papanice rain gauge. In blue rectangle the area interested by the 2012 landslide events.
 199 Daily (blue columns) and cumulative (red line and red numbers) rainfall values for: b) year 2012; c) February 2012; d)
 200 19-25 February 2012.



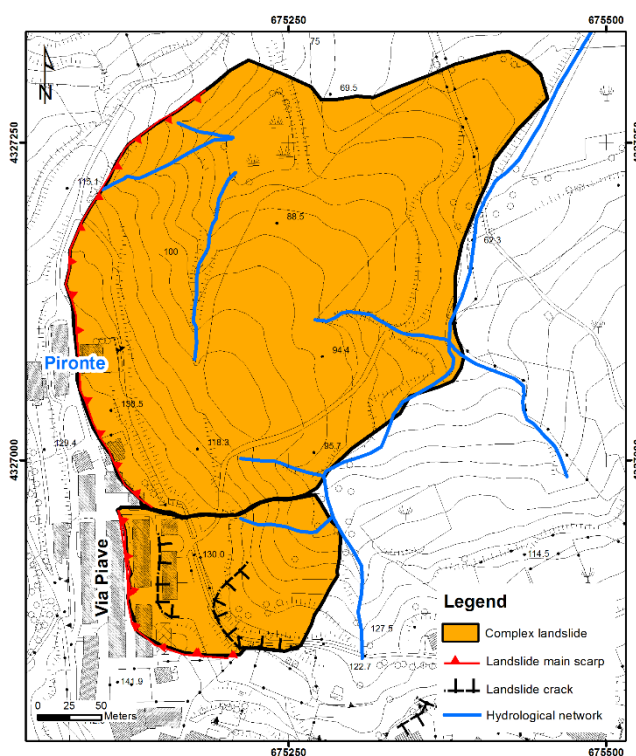
201
 202 **Figure 6** - Rainfall duration vs. cumulated event rainfall, conditions which resulted in shallow landslides in Calabria
 203 (red dots), and related threshold with a 95% confidence level. Shaded areas show uncertainties associated with the
 204 threshold. Blue dot = Papanice landslide. Modified from Vennari et al., 2014.

205
 206 **4. The Papanice landslide**

207 *4.1 Geomorphological field survey*

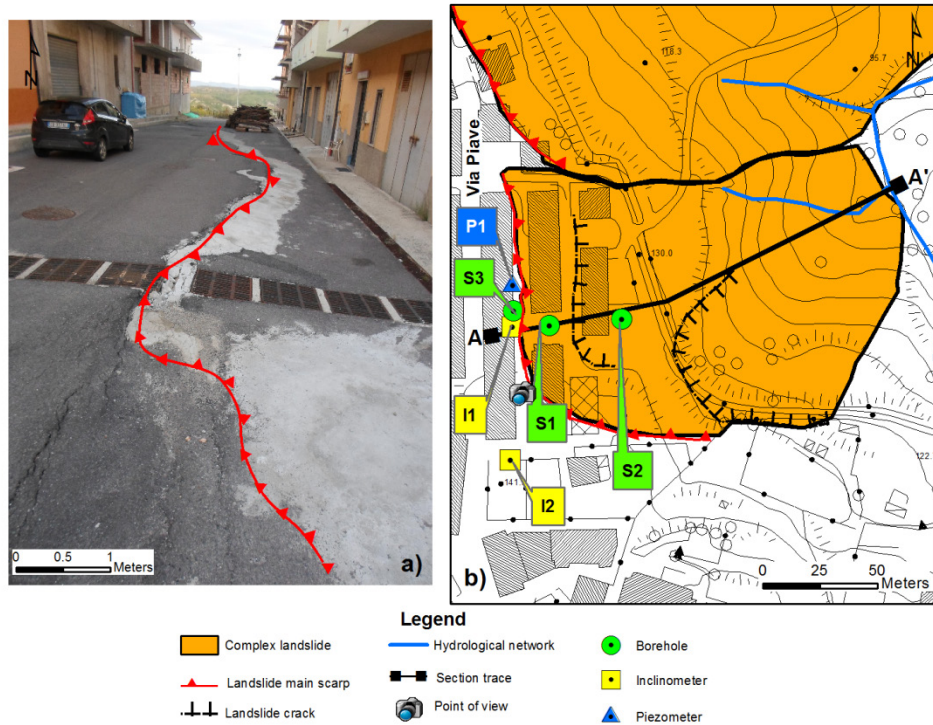
208 In order to investigate the long-term evolution of the past ground movements (Confuorto et al., 2015), further
 209 geological and geomorphological survey have been carried out allowing to redefine the landslide boundaries. The
 210 analysis started from the chronicle reports and the HSP Landslide Inventory Map redacted by the Calabria Regional
 211 Basin Authority (see Figure 3). The landslides (about 10 hectares large) occurring in the Pironte area can be considered
 212 as reactivations of pre-existing dormant landslides. Such reactivations took place on February 23, 2012, and their
 213 boundaries have been redefined according to the 2013 Fall and 2014 Summer field activities, whereas for the nearby
 214 landslides several evidences of the retrogressive trend movements have been shown (Figure 7). A general instability in
 215 the sector and along other slopes surrounding the settlement was already reported in the two years preceding the main
 216 event, according to ARPACAL (2013). The movement strongly damaged man-made structures located in the urban

217 area: fractures and tilting of the prominent houses have been documented as well as fractures in the road surface;
 218 moreover, the chronicles reported the evacuation of five houses. The displacement involved landfills due to human
 219 activities and the most superficial part of the Sant'Anna Synthem, made of strongly weathered silty clays. Within the
 220 SW landslide, the clearest evidence of the reactivation is represented by a ca. 140 m long fracture along Via Piave, a
 221 road located next to the crown area (Figure 8a). Longitudinally, a similar strong evidence is visible down to a dirt road
 222 just below the last row of houses; in addition, superficial signs have been recognized along the whole slope. When
 223 compared to the northern part of the landslide, where the displacement seems less intense, the SW landslide proves to
 224 be more affected by severe damage, as shown by gas and electric networks involvement, as well as fence and road signs
 225 sloped downwards.



226

227 **Figure 7.** Field survey landslide inventory map of the Pironte district



228

229 **Figure 8.** a) Landslide main scarp (Modified from Confuorto et al., 2015); b) Detail of the SW landslide and monitoring
 230 system installed after the 2012 main reactivation.

231 4.2 Monitoring campaign

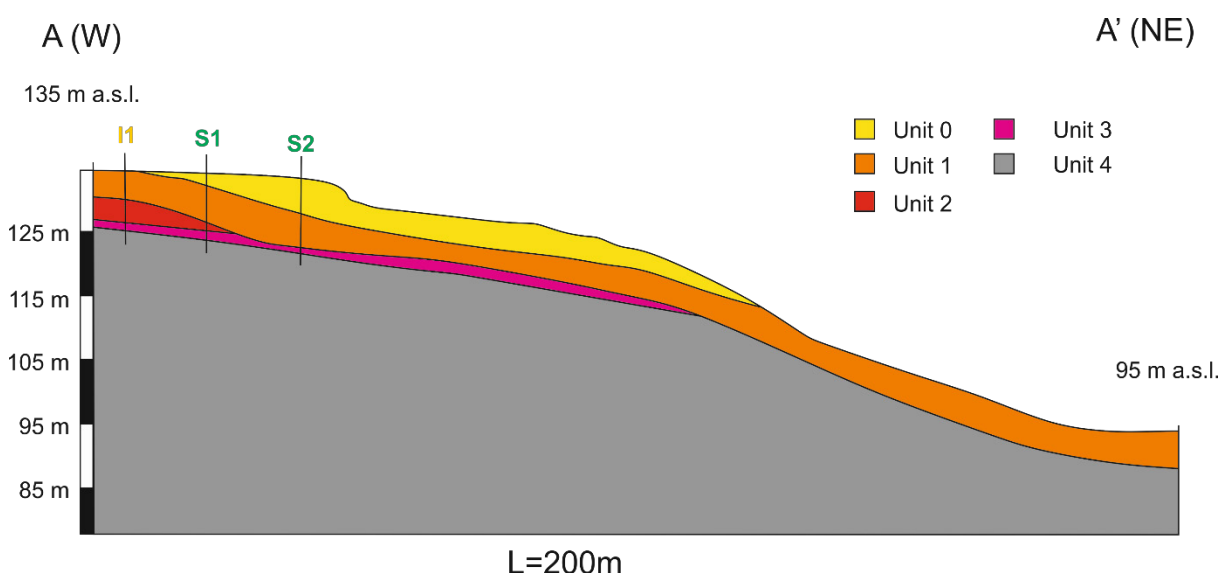
232 In order to investigate the SW landslide's evolution and to protect the buildings located outside the landslide area,
 233 ARPACAL set up a monitoring campaign immediately after the triggering phase occurred on February 23, 2012. It
 234 consisted of 6 boreholes (see Figure 8b) located along the crest of the landslide, which allowed to reconstruct a
 235 geological and geotechnical profile of the landslide (Figure 9). Different lithological units have been defined, whose
 236 main parameters are here reported:

- 237 - Lithotechnic unit 0: Chaotic material of the units 1, 2, 3;
- 238 - Lithotechnic unit 1: Mostly sandy and silty landfill; average geo-mechanical parameters: $\gamma=17-17.5 \text{ kN/m}^3$,
 239 $c=0.00 \text{ kPa}$, $\varphi=27-30^\circ$;
- 240 - Lithotechnic unit 2: Alternation of silty-clayey sands, clayey-sandy silts and sandy-clayey silts, avano-coloured
 241 (S. Anna synthem); average geo-mechanical parameters: $\gamma=19.8-20 \text{ kN/m}^3$, $c_u=0.00- 83.36 \text{ kPa}$, $c= 3.92- 13.72 \text{ kPa}$,
 242 $\varphi=26-30^\circ$;

243 - Lithotechnic unit 3: Silty-clayey cover with locally grey bands (weathered soil of the Cutro marly-clayey
 244 formation); average geo-mechanical parameters: $\gamma=19.8-20 \text{ kN/m}^3$, $c_u= 66.68- 88.26 \text{ kPa}$, $c= 12.75 - 18.63 \text{ kPa}$, $\phi=22-$
 245 25° ;

246 - Lithotechnic unit 4: Marly-silty clayey sedimentary substrate, grey-blue-coloured (Cutro marly-clayey
 247 formation); average geo-mechanical parameters: $\gamma=20-20.2 \text{ kN/m}^3$, $c_u= 107.87-176.52 \text{ kPa}$, $c= 17.65-27.46 \text{ kPa}$, $\phi=26-$
 248 27° ;

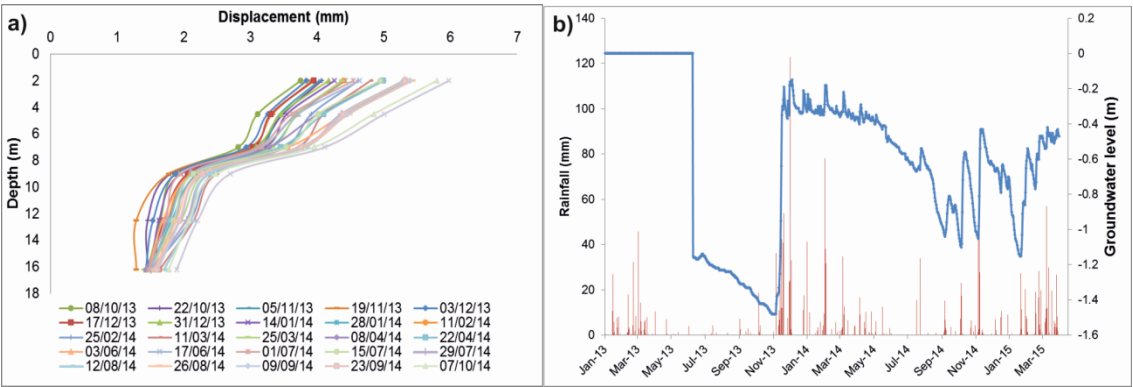
249 where γ is the volume unit weight, c_u the undrained cohesion, c the cohesion and ϕ the friction angle. The
 250 boreholes have been eventually equipped with two inclinometer chains and one piezometer. The inclinometer data have
 251 been acquired every fourteen day, during the time period October 2013 – October 2014.



252
 253 **Figure 9** - Geolithological section A-A'. The location of the section is shown in Figure 7. Keys to the Units are given in
 254 the text. I1 is the inclinometer, S1 and S2 are the two boreholes along the section.

255 Inclinerometers show a maximum displacement at the shallowest level (-8 m for I1 and -11 m for I2) of about 2 mm in the
 256 above-mentioned timespan, thus demonstrating that the area behind the landslide is not yet affected by considerable
 257 deformations (Figure 10a). Piezometer P1 (Figure 10b) is also located in proximity of the landslide and the available
 258 data are referred to daily measurements from January 1, 2013 to April 15, 2015. The comparison between piezometric
 259 readings and rainfall data, for the same time span, shows a good agreement: during dry and rainy periods, a decrease
 260 and increase, respectively, of the water table level can be noticed. It is worth pointing out that after mid-November 2013
 261 a sudden uplift of the piezometric level of about 1.2 m has been registered, reaching a very shallow depth (-0.2 m from
 262 ground surface) due to the leaking of urban sewage pipes, as reported by a first survey of ARPACAL (2013). After the

263 resolution of such event, the groundwater kept persistent at a very shallow level (between -0.2 and -0.4 m), because of
 264 the high precipitations (up to 115 mm on December 1, 2013). During springtime, rain occurrences explain little
 265 oscillations of groundwater level, which started to decrease as soon as the dry season begun (e.g. cumulative rainfall of
 266 51 mm during June and July 2014). In the final part of the analyzed time span, the piezometric levels showed large
 267 fluctuations, between 0.4 and 1.1 m, displaying again a correspondence with rainfalls (varying between several rainless
 268 days up to daily values of 55 mm).



269

270 **Figure 10** - a) Measurements of the inclinometer I1; b) Comparison between piezometric data from piezometer P1 (blue
 271 line) and daily rainfall at Papanice rain gauge (red).

272

273 5. PSI overview

274 5.1 Basic principles

275 Differential Interferometry SAR (DInSAR) (Gabriel et al., 1989; Massonet & Rabaute, 1993; Bamler & Hartl,
 276 1998; Wegmuller et al., 1998; Franceschetti & Lanari, 1999) is a very effective technique for the measurement of slow
 277 ground displacements, of structures and infrastructures, due to several phenomena, like subsidence, landslides,
 278 earthquakes and volcanic eruption. It enables to detect ground displacements with independence of the atmospheric
 279 conditions reaching a precision up to mm-accuracy. These techniques are based on the exploitation of the phase
 280 difference (interferograms) between two SAR images acquired at different times. Differential interferograms can be
 281 regarded as the sum of several terms (Hanssen, 2001) and DInSAR techniques are able to isolate, among such terms, the
 282 displacement contribution. Furthermore, PSI algorithms provide long temporal series of ground displacement by
 283 analyzing long stacks of differential interferograms in order to minimize the negative impact of decorrelation and
 284 atmospheric phase screen (APS). In this context, not every pixel of the illuminated scenario can be included in the
 285 processing since only those targets with a certain phase quality along the whole set of images or interferograms can be

selected as reliable, i.e, the so-called persistent scatterers. Regarding such selection, different approaches have been performed in this work. The different PSI solutions allow to work at different resolutions and with different nature of scatterers, being the coherence stability or the Amplitude Dispersion (DA), the most common pixels' phase quality estimators. In the first case, the interferometric quality of each pixel, for each multi-looked interferogram, is obtained from the estimated coherences, which are directly related with the standard deviation of the interferometric phase (Lanari et al., 2004). In the second case, the phase stability of targets along the data set is estimated from their DA, in those pixels presenting high signal-to-noise ratio (SNR) values (Ferretti et al., 2000). The coherence stability pixel selection criterion is more suited for the analysis of natural environments with distributed scatterers and performs well even when a reduced number of SAR images is available, while the DA pixel selection criterion, which works at pixel level, is ideal for the identification of point-wise scatterers, such as man-made structures in urban scenarios, however it requires a large number of images to reach a reliable selection. The former approach, which works with distributed scatterers, requires the selection of differential interferograms limiting the maximum value of temporal and spatial baselines in order to reduce decorrelation phenomena. For this reason this method is typically addressed as SBAS. The latter approach, which exploits the nature of point-like scatterers are theoretically not affected by speckle noise and can work with all possible combinations and it is typically referred to as PS. In order to select point-wise scatterers without relying on the amplitude of SAR images, another estimators, such as the Temporal Sublook Coherence (TSC) (Iglesias et al., 2014b) used in this paper, has been recently introduced. This method allows exploiting the spectral properties of point-like scatterers and, therefore, working at high-resolution in scenarios with high dynamics in the temporal evolution of amplitude and/or when a reduced number of images are available (Iglesias et al., 2015). Once a selection of persistent scatterers candidates (PSCs) is obtained, different PSI configurations are available (Ferretti et al., 2001; Berardino et al., 2002; Arnaud et al., 2003; Mora et al., 2003; Werner et al., 2003; Lanari et al., 2004; Duro et al., 2005, Costantini et al., 2008; Hooper, 2008; Prati et al., 2010; Ferretti et al., 2011b and Sowter et al., 2013). The objective of such approaches is the precise estimation of the linear displacement, but also the separation of APS and non-linear displacement contribution to obtain precise time-series of displacement over the PSCs previously selected. Most of these approaches are composed by a first step devoted to estimate the linear contribution of the differential phase, i.e, the linear component of ground displacement and residual topographic error remaining in the differential interferograms due to the lack of precision in the DEM employed during their generation. Such step is especially important in mountainous environments, where the topographic error contribution can be significant and can affect the final results if it is not estimated and compensated for. This linear phase contribution is hence employed to ease the phase unwrapping (PhU) processing and finally a filtering process is carried out in order to separate the APS contribution from the non-linear displacement contribution, taking advantage of the particular temporal and spatial frequency behavior of these

317 two components. In mountainous areas, where landslides typically occur, the separation of APS and non-linear
318 displacement contribution require further analysis. This issue is analyzed in detail in the following Section.

319 5.2 *APS compensation at X-band over areas with steep topography*

320 The mitigation of the negative impact of atmospheric phase screen (APS) results of crucial importance to ensure
321 the reliability of PSI products. The contributions of atmospheric artifacts at X-band in areas with steep-topography,
322 where landslide typically occur, is significant and deserve more explanation. The approach followed in this paper is put
323 forward. These phase anomalies are caused by refractivity gradients in the troposphere (lower part of the atmosphere:
324 from sea level to about 10-11 Km altitude), mainly produced by inhomogeneity in the temperature, pressure and water
325 vapor content, and by dispersive effects in the ionosphere (upper part of the atmosphere: from about 85 km to 600 km),
326 mainly produced by variations of Total Electron Content (TEC). Dealing with ionospheric effects, which contribution is
327 significant for low-frequency SAR sensors (such as the L-band ALOS-PALSAR sensor) is beyond the scope of this
328 paper, which is focused on the exploitation of high-resolution X-band sensors for landslide monitoring applications.
329 Leaving aside the ionospheric contribution, it is common to separate APS into one component related to turbulent
330 mixing processes and other to tropospheric stratification:

331 • Turbulent mixing comes from mixing processes in the inhomogeneous atmosphere, i.e, at the lower part of the
332 troposphere (up to 2-3 km above ground). This APS contribution is directly related with the day-to-day weather, such as
333 wind, rain, snow, fog, etc., and produces significant changes in the signal path delay. The negative impact of this
334 component is mitigated exploiting the spectral differences between the displacement component and APS through the
335 use of spatio-temporal filters (Ferretti et al., 2000; Hanssen, 2001). Going into more detail, turbulent atmosphere may
336 be defined as a stochastic process with a low spatial frequency behavior (geo-statistically characterized by a specific
337 varioagram with 1 km correlation window (Hanssen, 2001) and completely random along the temporal axis). Regarding
338 the spatial behavior, this means that the shorter the distance between two points affected by turbulent atmosphere, the
339 more similar their phase values will be. Regarding the temporal behavior, for a given pixel (belonging to an image, not
340 to an interferogram), APS can be considered as a white process since atmospheric conditions change randomly for each
341 acquisition date. Contrarily, non-linear displacement contribution is considered to present a narrower spatial correlation
342 window compared with APS and to behave smooth along the temporal axis.

343 • Tropospheric stratification results from temporal variations in the vertical refractive index profile. In other
344 words, the vertical stratification of the troposphere in different layers (with different propagation velocities due to the

345 different refraction index at different elevations) leads to an additional phase delay, superimposed to the phase
346 component of displacement.

347 The approach followed in this work is based on adapting spatio-temporal filters, typically used to compensate
348 turbulent mixing, applying at this time an extra reduction of the spatial low-pass filter kernel in order to face the
349 possible rapid fringes related with tropospheric stratification at X-band. As seen, turbulent processes are typically
350 characterized by having a low spatial frequency behavior, typically 1 km correlation window (Hanssen, 2001). In order
351 to compensate tropospheric stratification at X-band, the kernel size of low-pass filtering should be reduced to 100-200
352 meters.

353 The final results, both linear term of deformations and the time series, are affected by the uncompensated DEM
354 errors and atmospheric artefacts. The impact of the errors is not easy to evaluate as it depends on many different factors:
355 the topography, the distribution of temporal and spatial baselines, the atmospheric artefacts, etc. and it is beyond the
356 scope of the paper. The PhD thesis of Centolanza (Centolanza, 2015) covers in detail how the errors propagate from the
357 data to the final results.

358 *5.3 SAR data*

359 The PSI analysis of the Papanice landslide has been carried out using StripMap TerraSAR-X images, covering two
360 different time spans, April 2008-June 2010 for the pre-failure phase and October 2013-October 2014, for the post-failure
361 phase. Both stacks have been obtained thanks to the participation in DLR GEO1589 and GEO2641 proposals, aiming at
362 the exploitation of satellite interferometric data for landslide studies. In particular, the first stack consisted of 66 and 67
363 SLC images acquired between April 2008 and June 2010 in StripMap mode ($3\text{ m} \times 3\text{ m}$ ground resolution), along
364 ascending and descending pass, respectively, with mean incident angle of 30° , HH polarization and repeat cycle of 11
365 days. The second one encompasses 34 ascending and 39 descending SLCs, with a mean incident angle of 30° , HH
366 polarization and 11 days repeat cycle. Finally, a Digital Terrain Model (DTM) with $5\text{ m} \times 5\text{ m}$ resolution cell has been
367 used during the PSI processing in order to remove the topographical phase contribution and to georeference the results.

368 **6. PSI results**

369 *6.1 Pre-processing analysis*

370 PSI methods have shown great potential for landslides monitoring and detection (Wasowski & Bovenga, 2014).
371 However, the application of PSI techniques is still characterized by some limitations, especially in the estimation and
372 the detection of the measurement points (Colesanti et al., 2006). The mapping and monitoring of ground displacements

often show certain restrictions, even with VHR images, depending not only on the sensor's characteristics, but also on the geometrical and geomorphological features of the area of interest. Three geometric distortions, due to the combination of geometry of the acquisition and of the slope of interest, notoriously characterize the SAR imagery: foreshortening, layover and shadowing (Kropatsch & Strobl, 1990). In the scientific community, new pre-processing tools have been developed in order to assess the detection and the quality of the targets. Several procedures have been established in the last six years (Notti et al., 2010, 2014; Plank et al., 2013).

The R-Index equation is a model which is able to calculate the target quality of an area by taking into account the radar geometry, the slope angle and dip orientation (Notti et al., 2010, 2014). The R-Index equation is the ratio between the slant range and the ground range, starting from the geometry of the sensor and the geometry of the surface of analysis. Dip slip and the aspect of the slope, both derivable from a DTM, belong to this last category. The most suitable geometry which allows to have pixels best quality occurs when the slope is parallel to the Line-of-Sight (LOS), corresponding hence to the maximum value of the R-Index, equal to 1; on the contrary, the lowest value of the R-Index comes about in occurrence of foreshortening ($0 < \text{R-Index} < 0.4$) or layovering ($\text{R-Index} < 0$). R-index was used to select the best-suited imaging geometry for Papanice area landslide monitoring. It has been applied to both TerraSAR-X stacks, showing the following results: the landslide's slope, on the ascending orbit, corresponds to pixels with very good quality (≥ 0.4 on average) (Figure 11a). On the contrary, the descending orbit is characterized by poor quality of the pixels (< 0.4 on average), so that this stack cannot be considered suitable for PSI procedures.

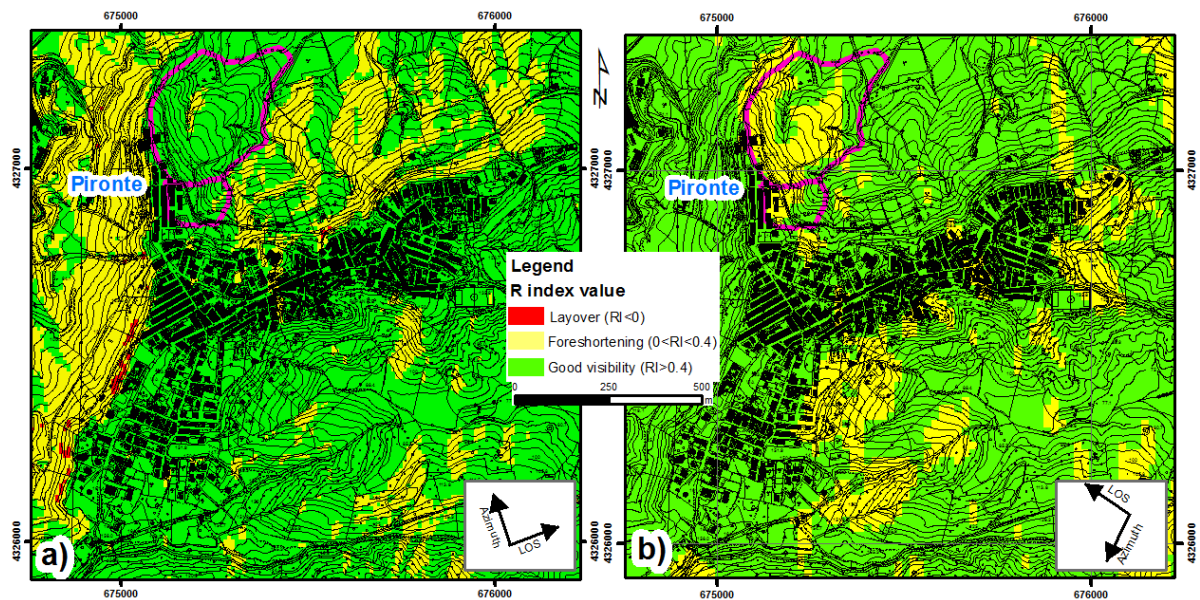


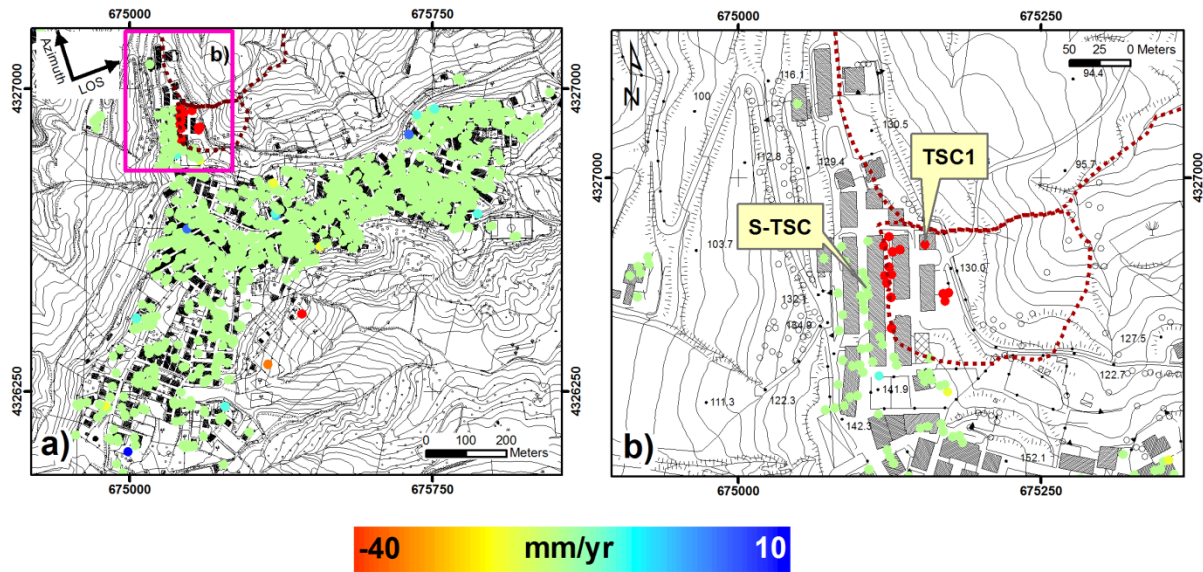
Figure 11 – R-Index computation for ascending (a) and descending (b) orbits. Red colors show the layover areas (R-Index < 0), yellow areas show foreshortening ($0 < \text{R-Index} < 0.4$), green areas mark a good visibility ($\text{R-Index} \geq 0.4$). Landslides are reported in purple line.

394 6.2 Pre-failure stage analysis

395 The analysis of the pre-event ground deformation has been successfully carried out using two different software
396 packages with the same pixel selection criteria (PS-like), as reported in Confuorto et al. (2015), in order to investigate
397 and monitor the precursor stages of the landslide involving the Pironte neighborhood in Papanice; the two software are
398 SUBSOFT and SARscape™.

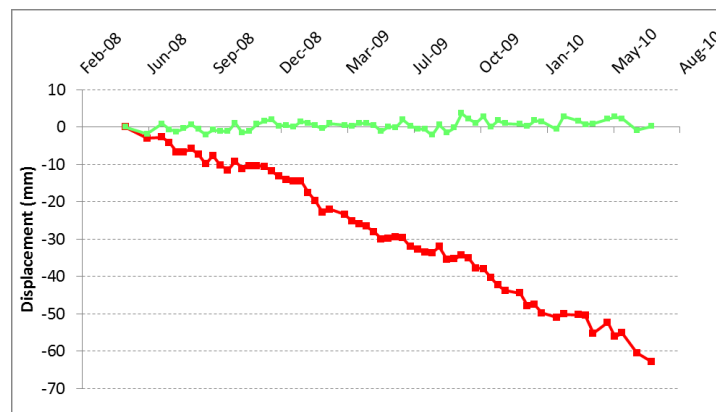
399 The SUBSOFT processor has been developed by the Remote Sensing Lab of the Universitat Politècnica de
400 Catalunya of Barcelona, Spain, using the Coherent Pixel Technique (CPT, Mora et al., 2003; Blanco-Sanchez et al.,
401 2008). For the Papanice landslide, a new implementation, the Temporal Sublook Coherence (TSC) (Iglesias et al.,
402 2015), has been exploited. The latter allows to select point-like scatterers analyzing the spectral properties of the
403 scattered signal. The advantage with respect to the conventional PS selection, based on the amplitude dispersion, is that
404 there is no need of applying a radiometric calibration. Hence, in this case, the pixel selection is carried out exploiting
405 the spectral properties of point-like scatterers. Further description of the technique can be found in Iglesias et al. (2015).

406 The SUBSOFT results are reported in Figure 12, where points referable to the landslides are more than one
407 hundred, and shown in red. The average velocity (where positive values mean movements toward the satellite, while
408 negative values refer to movements away from it) obtained with the CPT-TSC analysis is of -27.7 mm/yr, while the
409 maximum rates, located in the NW sector of Via Piave landslide, are of -36.0 and -35.6 mm/yr. Other high velocities
410 can be found along the main scarp. The lowest values of movement are located in the southern sector and downslope,
411 with a minimum rate of -14.8 mm/yr. In order to evaluate the reliability of the processing and the expected error,
412 displacement standard deviation of the stable points (behind the landslide affected area) has been calculated, resulting
413 equal to 1.5 mm. Figure 13 shows time-series of displacement for a stable point (S-TSC) and for a point within
414 landslide affected area (TSC1).



415

416 **Figure 12** - a) Displacement rate map obtained with the CPT-TSC algorithm for the time interval 2008-2010. In the
 417 purple rectangle, a zoom-in of the area of interest (b). Landslides have been reported in brown-dashed line. The points
 418 S-TSC and TSC1 have been selected for the time series analysis (Figure 13). Modified from Confuorto et al. (2015).

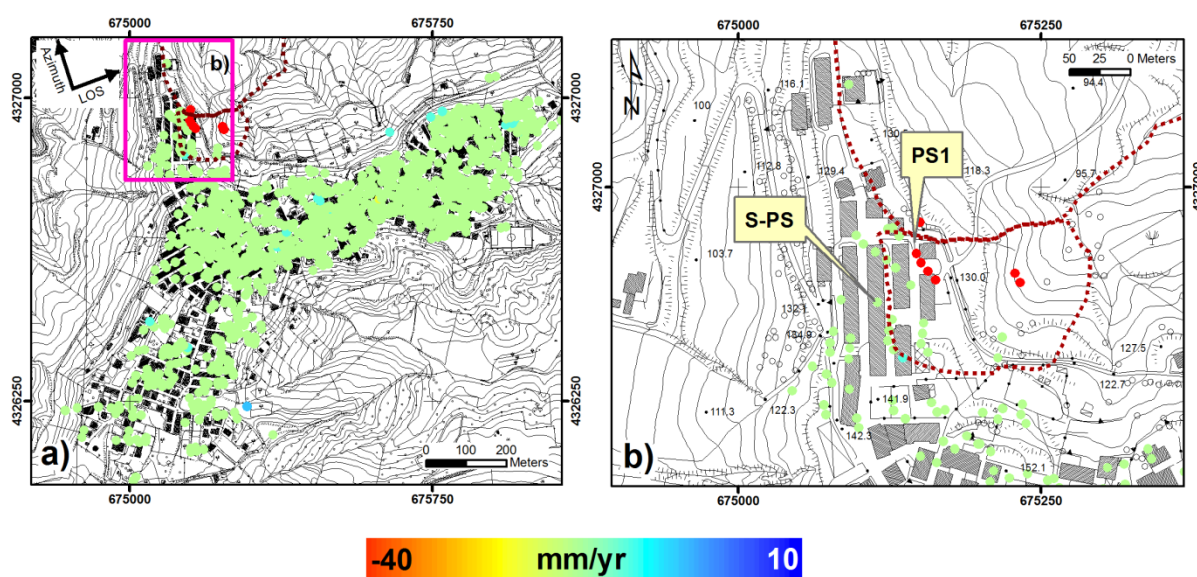


419

420 **Figure 13** – Time series of displacement of the points S-TSC (green) and TSC1 (red). Modified from Confuorto et al.
 421 (2015).

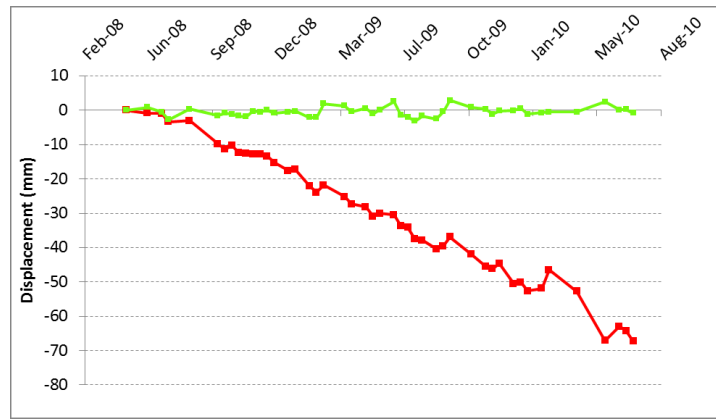
422 In order to obtain SARscape™ results, a procedure to improve the PS processing had to be carried out, splitting
 423 the stack into two periods (1st period, April 2008 – August 2009; 2nd period, April 2009 and June 2010) and imposing
 424 a spatial baseline threshold of ± 100 m, as done in Confuorto et al. (2015). The experiments showed that a splitting of
 425 the data set into two overlapping stacks strongly increased the number of persistent scatterers compared to a scenario
 426 where it has been processed the entire data set in a single step. By analyzing a shorter time period the number of points
 427 which are characterized by a high coherence is higher than the number of points showing a high coherence over the
 428 entire period analyzed. The two sub-periods overlap each other to guarantee a meaning-full analysis of the measured

429 displacements. In the first period, 7 PSs have been identified in the landslide area (Figure 14). The exact location, inside
 430 the landslide perimeter, is in the NW sector and in the middle part of it, and the average velocity is of -25 mm/yr along
 431 the LOS. The highest displacement rates are all located in the NW sector of the landslide, reaching a top value of -32.1
 432 mm/yr. The second period of analysis is based on 27 images, and in this case, 1543 PSs have been recognized.
 433 However, just one is ascribable to the movement, and also in this case it is situated in the NW part, along the main
 434 scarp, showing a displacement rate of -32.1 mm/yr. Both results showed the potentiality of DInSAR to detect precursor
 435 stages of a future slope failure. Also in this case, in order to evaluate the reliability of the processing and the expected
 436 error, displacement standard deviation of the stable points (behind the landslide affected area) has been calculated,
 437 resulting equal to 1.2 mm. Figure 15 shows time-series of displacement for a stable point (S-PS) and for a point within
 438 landslide affected area (PS1).



439

440 **Figure 14** - a) Displacement rate map obtained with the PS (1st period of analysis) algorithm for the time interval 2008-
 441 2009. In the purple rectangle, a zoom-in of the area of interest (b). Landslides have been reported in brown-dashed line.
 442 The points S-PS and PS1 have been selected for the time series analysis (Figure 15). Modified from Confuorto et al.
 443 (2015).

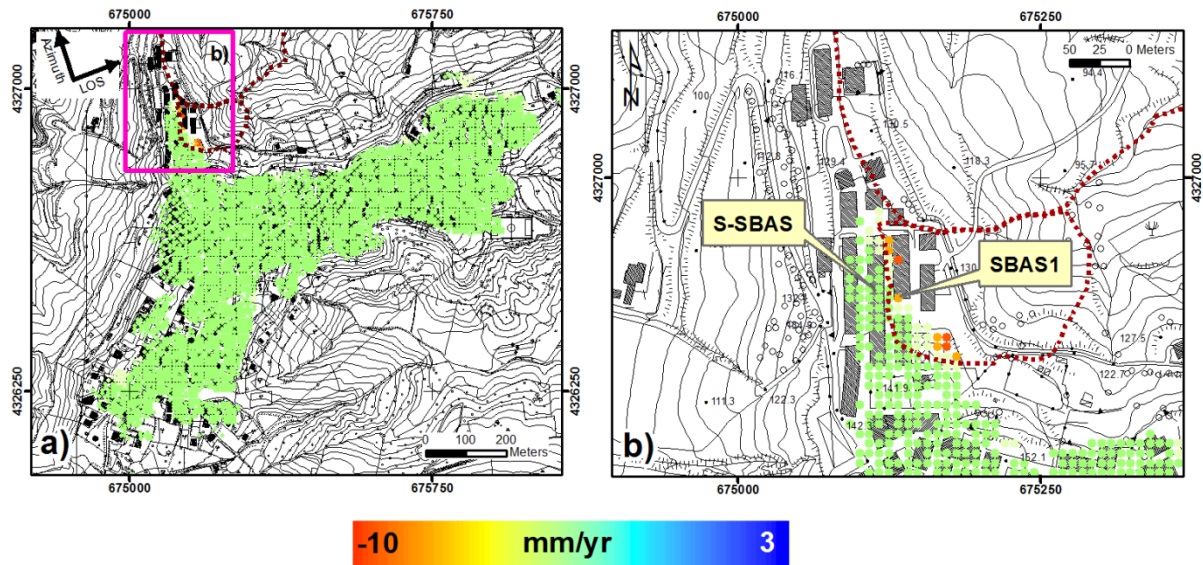


444

445 **Figure 15** - Time series of displacement of the points S-PS (green) and PS1 (red). Modified from Confuorto et al.
 446 (2015).

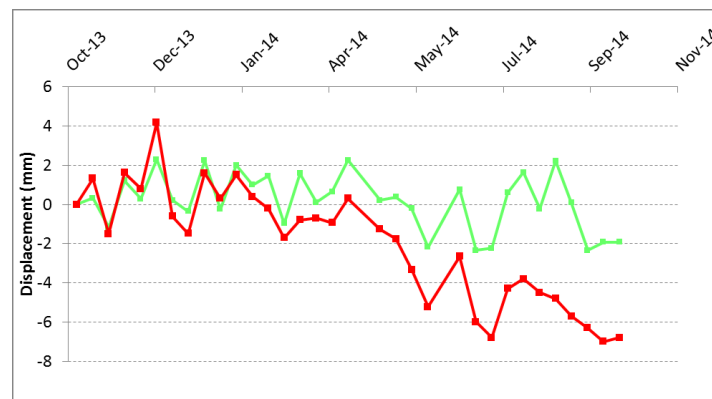
447 6.3 Post-failure stage analysis

448 The post-failure stage analysis was limited to the TerraSAR-X ascending stack, because of the inadequate R-Index
 449 values (Figure 11), as for the previous dataset (2008-2010). The elaboration of the TerraSAR-X imagery has been
 450 carried out by means of SUBSOFT and SARscape™ software. The former aim was to analyze the displacement on a
 451 larger scale with the application of the SBAS algorithm, which is more suitable for analysis at a less detailed scale and
 452 on regional context. The SARscape™ software has then been tested with SBAS technique for the assessment of the
 453 post-failure phase. In this case, according to the standard procedure, two values of temporal and spatial baseline have
 454 been selected, 100 days and the 2.5% of the critical spatial baseline (ca. 5000 m) respectively, which allowed to select
 455 143 interferograms for the final estimation. More than 4000 points have been then recognized (Figure 16), showing two
 456 different concentrations of points involved in the displacement: on the NW sector, 12 points can be referred to the
 457 landslide movement, and are located within the border and along the scarp of the main landslide documented during
 458 field activities, with an average velocity of -4.5 mm/yr. Moreover, another cluster located in the SE part, with average
 459 displacement rate of -4.8 mm/yr and maximum value of -8.3 mm/yr, has been identified. All values are referred to the
 460 LOS. As previously made, in order to evaluate the reliability of the processing and the expected error, displacement
 461 standard deviation of the stable points (behind the landslide affected area) has been calculated, resulting equal to 1.0
 462 mm. Figure 17 shows time-series of displacement for a stable point (S-SBAS) and for a point within landslide affected
 463 area (SBAS1).



464

465 **Figure 16** - a) Displacement rate map obtained with the SBAS method for the time interval 2013–2014. In the purple
 466 rectangle, a zoom-in of the area of interest (b). Landslides have been reported in brown-dashed line. The points S-SBAS
 467 and SBAS1 have been selected for the time series analysis (Figure 17).

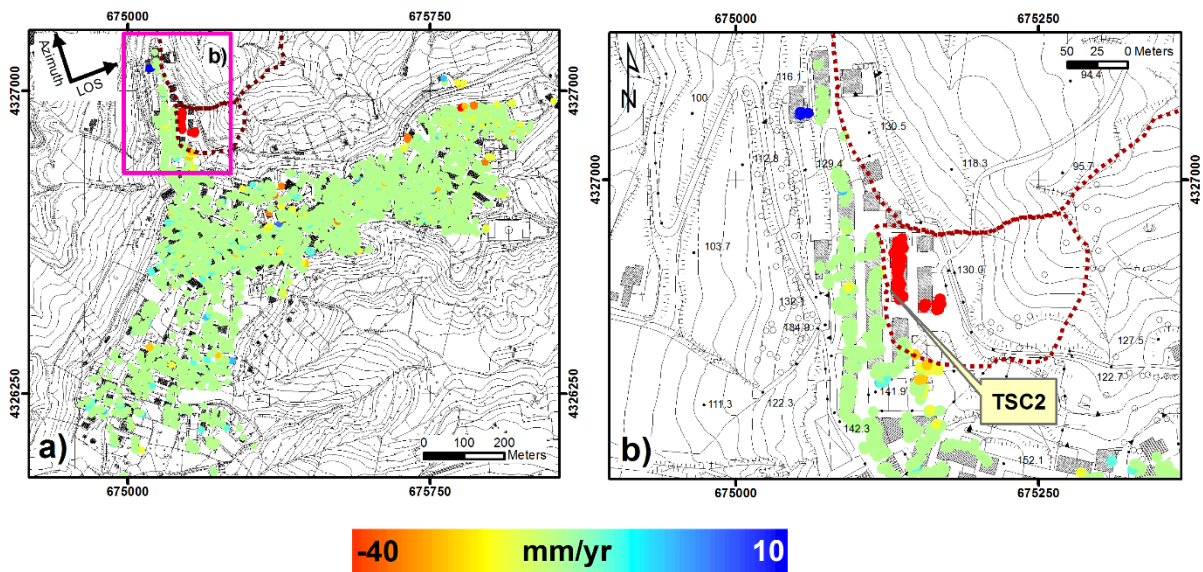


468

469 **Figure 17**- Time series of displacement of the points S-SBAS (green) and SBAS1 (red).

470 CPT-TSC has then been used on a final selection of 34 images, with a temporal interval of exactly one year
 471 (October 2013 – October 2014) in order to verify the above-mentioned results reliability, i.e. to understand whether the
 472 movement has truly slowed down in the post-failure phase, or if the SBAS tend to underestimate velocities. For the final
 473 pixel selection, a TSC threshold 0.7 has been set, selecting more than 14000 targets (Figure 18), characterized by a
 474 phase standard deviation of about 20° which corresponds to a displacement standard deviation of about 1.5 mm.
 475 According to this elaboration, the landslide seems to confirm the pre-failure high velocities, showing a cluster of points
 476 with relatively high displacement rates, both in the NW sector, already classified as the fastest sector of the landslide in
 477 the previous period, and in the southern one, where beforehand no displacement was identified. In this period the

478 movement rates are higher, with an average displacement of -40 mm/yr in the NW sector, of about -35 mm/yr in the
479 central sector, while mean values of -5.8 mm/yr are detectable in the SE sector.

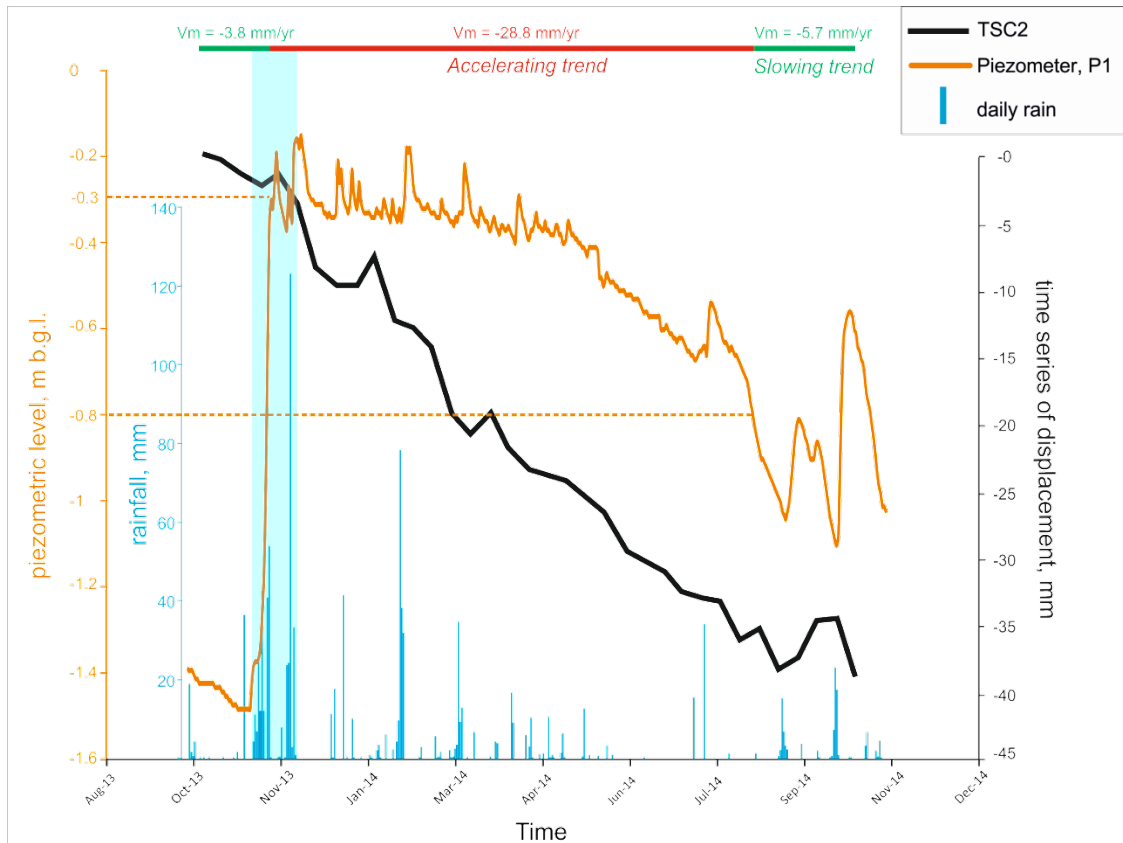


480

481 **Figure 18** - a) Displacement rate map obtained with the CPT-TSC method for the time interval 2013–2014. In the
482 purple rectangle, a zoom in of the area of interest (b). Landslides have been reported in brown-dashed line. The point
483 TSC2 has been selected for the time series analysis (Figure 19).

484 **7. Slope stability analysis**

485 The rise and the very shallow depth of the piezometric level during the considered time-span can surely represent
486 an important instability factor. According to the considered time series (point TSC2, see Figure 18), derived from the
487 CPT-TSC processing and chosen in proximity of the piezometer P1, the activation of the movement seems to occur
488 when the groundwater surface reaches 0.3 m below the ground surface (Figure 19). Starting from this assumption, a
489 slope stability analysis of the study area has been carried out considering the water table level at such depth, in order to
490 identify the most significant parameters which brought this slope to instability.



491

492 **Figure 19** - Comparison between piezometric and rainfall data with time series obtained with the CPT-TSC algorithm.
 493 On the top bar, the average trends of the TSC2 time series. The average LOS velocities are shown for the slowing and
 494 accelerating trends. Dashed lines show the connection between piezometric level and acceleration and deceleration of
 495 the ground movement. The blue shaded column is for the rainy period between November 11, 2013 and December 4,
 496 2013, correspondent to a rapid rise of piezometric level.

497 The slope analysis has been performed with Slope®, a software by GEOSTRU
 498 (<http://www.geostru.com/EN/Slope-stability-analysis.aspx>), which exploits the limit equilibrium method. The final aim
 499 is to obtain the Safety Factor (SF) of a slope, referring to a theoretical model based on the slope stratigraphy and
 500 evaluating the global stability through the relationship between maximum shear strength and the stresses acting on the
 501 slope surface:

$$SF = \frac{T_{max}}{T_{mob}} \quad (1)$$

502 with T_{max} representing the maximum shear strength available and T_{mob} being equal to the shear stress mobilized.

503 The limit equilibrium condition is attained when $T_{max} = T_{mob}$, hence when $SF = 1$. Consequently, a slope can be
 504 considered stable when $SF > 1$ as well as unstable when $SF < 1$. Such analysis takes into account a representative
 505 section of the slope, as shown in Figure 8b. In detail, two different periods have been considered: a) configuration of the

slope before the 2012 movement, obtained from the Regional Technical Cartography; b) configuration of the slope after the 2012 landslide, obtained by a topographic survey done after the event by ARPACAL, in November 2012. The comparison between such two profiles shows that the slope's morphology is substantially unchanged, even considering the landslide event (Figure 20).

Water table in the pre-event condition has been considered at -0.3 m from the ground level and continuous for all the profile. Such hypothesis can be considered reliable, according to rainfall and piezometric data. Furthermore, the comparison between the time series derived from the PSI elaboration and the piezometer P1 clearly shows that the activation of the displacement took place when the water table level increased up to such height (Figure 19). As to strength parameters, chosen values are the residual ones and they were obtained by means of back-analysis procedure, varying the pre-event friction angle value up to the value of mobilized strength. The stability analysis has been performed according to the Janbu method (Janbu, 1954). Thereby, the landslide body was divided into single elements and for each of them the equilibrium between forces and strength was calculated, thus obtaining the global SF. In order to characterize the terrains, a simple constitutive model was adapted, based on Mohr-Coulomb theory (Mohr, 1914), entering volume unit weight, cohesion and friction angle values.

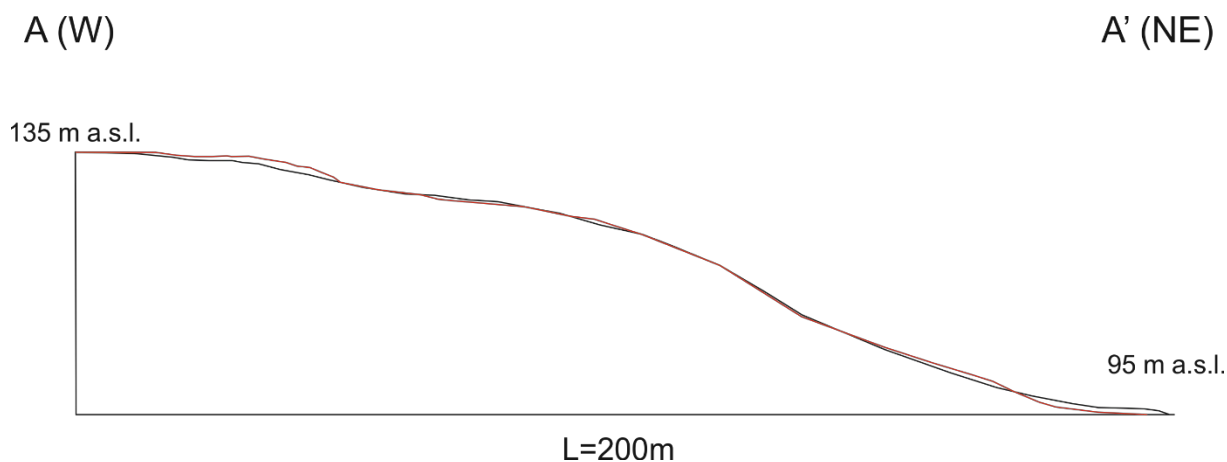
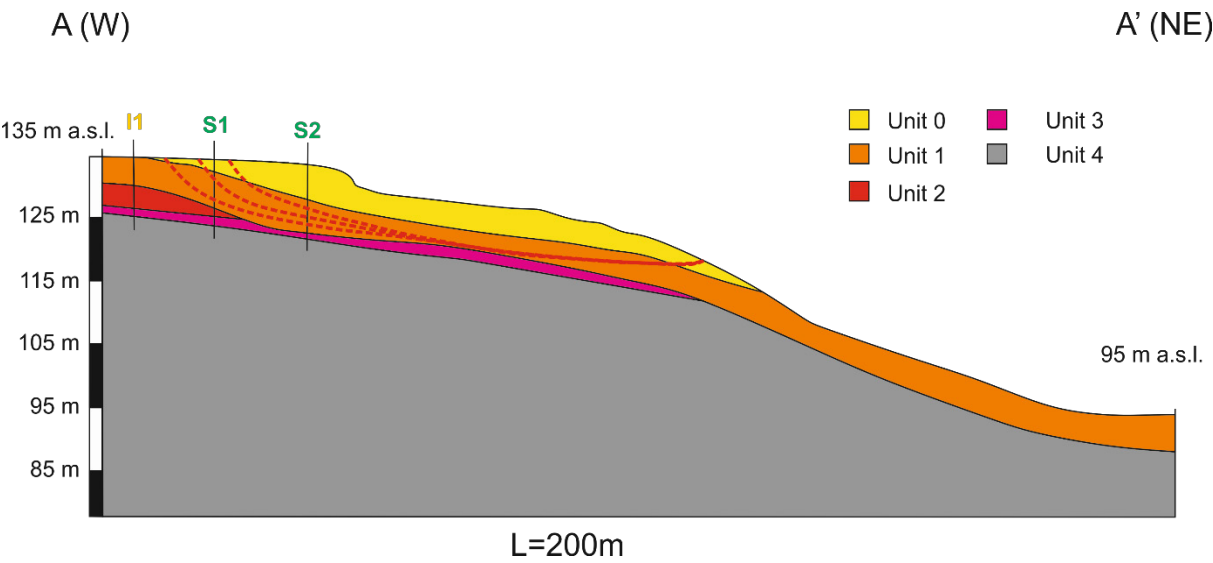


Figure 20 - Profiles of the slope of analysis: pre-event configuration (red line), post-event configuration (black line). The location of the section is shown in Figure 8b.

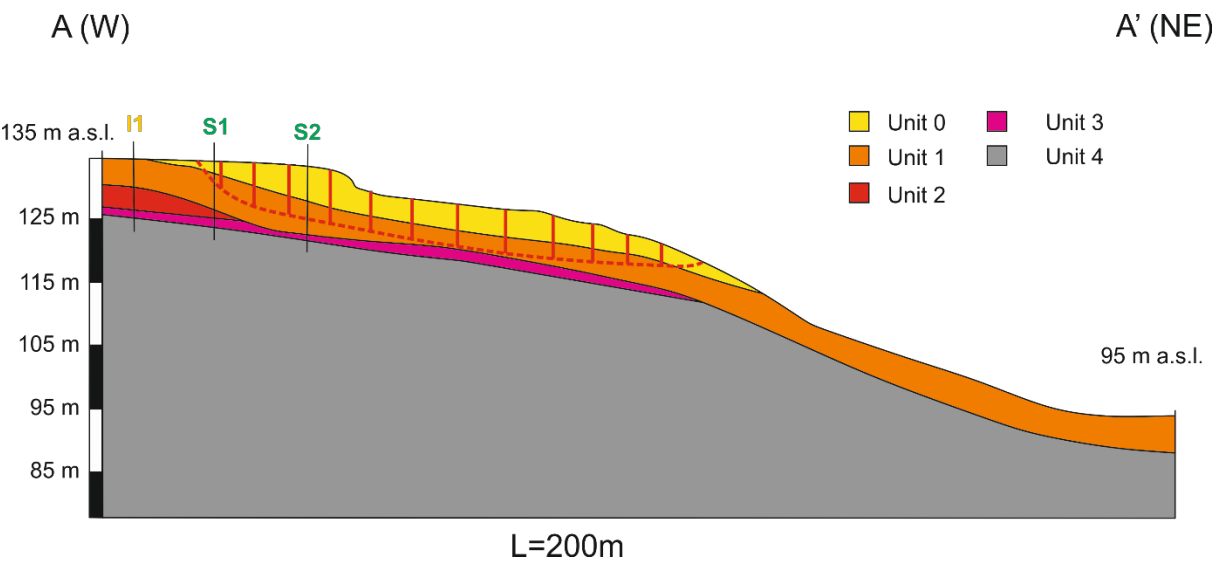
First, a back analysis based on the pre-event profile has been carried out, in order to determine the slope's condition at the 2012 activation. Three different slip surfaces have been hypothesized (Figure 21). On the base of the available information about the slip surface (cfr. section 4.2), a depth of about 8 m has been assumed, with the edge in proximity of Via Piave (according to inclinometer data and fractures in the roadway observed during the field survey, respectively). Analyses were carried out changing the value of the residual friction angle of the units involved in the landslide, while all the other parameters were kept unchanged. Such procedure calculated that the $SF=0.96$, less than 1

529 (limit equilibrium condition), is reached when $\phi'_r = 17^\circ$, which represents the shear strength of the units mobilized
 530 along the specific slip surface.



532 **Figure 21** - Back-analysis simulation, where the three hypothetical slip surfaces are represented with red-dashed lines.
 533 I1 is the inclinometer, S1 and S2 are the two boreholes along the section.

534 The next step was to verify the conditions in post-event configuration, starting from the same residual friction
 535 angle ($\phi'_r = 17^\circ$). An analogue stability analysis has been carried out on the post-event configuration (Figure 22).



537 **Figure 22** - Stability analysis on the post-event profile. The slip surface identified is indicated in red-dashed line. The
 538 vertical red lines represents the different slices drew following Jambu method. I1 is the inclinometer, S1 and S2 are the
 539 two boreholes along the section.

540 The surface highlighted in Figure 22, obtained by this procedure, is very similar to the one presumed for the pre-
541 event phase and assumes a value of $SF = 0.97$ when the water table lies at -0.3 m from the ground surface, thus posing a
542 critical issue for the current stability of the slope. Moreover, also according to the PSI analysis, the area appears to be
543 still moving, even after the triggering phase. As a consequence of these results, in order to increase the SF and to
544 guarantee the maximum stability of the slope, a possible solution could be to operate on the water table level. A
545 suggestion could be the implementation of drainage trenches along the whole landslide body, trying to decrease the
546 groundwater level until at least 0.8 m below the surface. In such condition, the SF would be equal to 1.07, therefore
547 guaranteeing the stability of the slope. Time series analysis confirms that the stability of the slope is obtained through
548 the lowering of the water table level: a slowdown of the movement can be noticed when the groundwater level reaches -
549 0.8 m from the ground surface (Figure 19), thus validating the well-known connection between groundwater presence
550 and triggering/reactivation of slow-moving landslides.

551 **8. Discussion**

552 Piezometric data allowed to investigate the relationship between slope movements and groundwater level. The
553 comparison between PSI time series and rainfall data clearly shows accelerations soon after abundant precipitations, as
554 well as decelerations during dry periods (Figure 19). For instance, during a very rainy period which occurred at the end
555 of 2013 (275 mm between November 18 and December 1), the time series derived from the CPT-TSC processing shows
556 an acceleration of the displacement, starting from December 3. In the same time-span, the piezometric level suddenly
557 increased (Figure 19), as a response to heavy rainfalls (275 mm in 14 days) and the presumable leaking of water pipes;
558 water level increases more than 1 m (from -1.4 to -0.2 m), reaching a very shallow depth. After that, the displacement
559 seems to undergo a drastic acceleration, starting from December 3, 2013. In the subsequent phase, the piezometric level
560 keeps constant at a very shallow level, between -0.2 and -0.4 m, with small oscillations due to the variable intensity of
561 the daily precipitation. During this time-span, the displacement also keeps persistent, with small accelerations soon after
562 intense rainfalls. Starting from mid-May 2014, this superficial aquifer drops at least of 0.2 m, throughout the dry season,
563 and simultaneously the movement slows down (average LOS velocity of -5.7 mm/yr), as shown in the time series. In
564 the last part of the analyzed period, water level went through severe oscillations, due to very high daily rainfalls, and
565 accordingly the time series continue to show a rapid response of the ground to such events. However, it must be
566 specified that the time response to rain can be quite variable, owing to several factors, such as the geotechnical
567 properties of landslide terrains, the morphology of the slope, the depth and volume of the landslide body, etc.

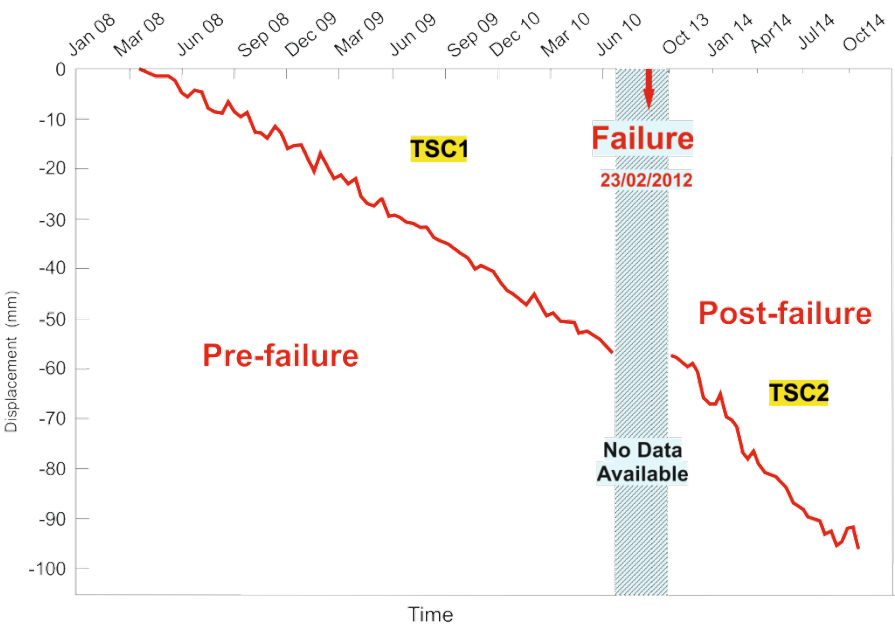
568 After the first results presented in Confuorto et al. (2015) one of the main objectives was the need of a more
569 complete and accurate analysis of the studied slope in order to investigate predisposing factors and the possible

570 evolution of the movement by means of remote sensing techniques and with the support of conventional methods. The
571 whole time-span of observation along the slope of interest showed a total displacement of almost 10 cm in more than 3
572 years of monitoring (Figure 23). The first part of the present study showed how PSI methods are able to detect, even at
573 a very local scale, displacements and precursor stages of slow-moving landslides. To achieve this goal, two different
574 kinds of PSI algorithms were applied: the CPT-TSC on the SUBSOFT processor and the SBAS on SARscape. The
575 availability of different PSI techniques allowed to compare a PS-like method with an SBAS-like one, to evaluate their
576 performance on such phenomena and finally highlight possible differences or similarity in the results. The first results
577 obtained in Confuorto et al. (2015) demonstrated the high accuracy of two PS-like techniques in such settings. In this
578 work SBAS seems to underestimate the velocities of the displacement in the landslide area, with respect to the pre-
579 failure stage, and the comparison with field survey, during which evidences of movement with considerable
580 displacements have been reported, confirms this thesis.

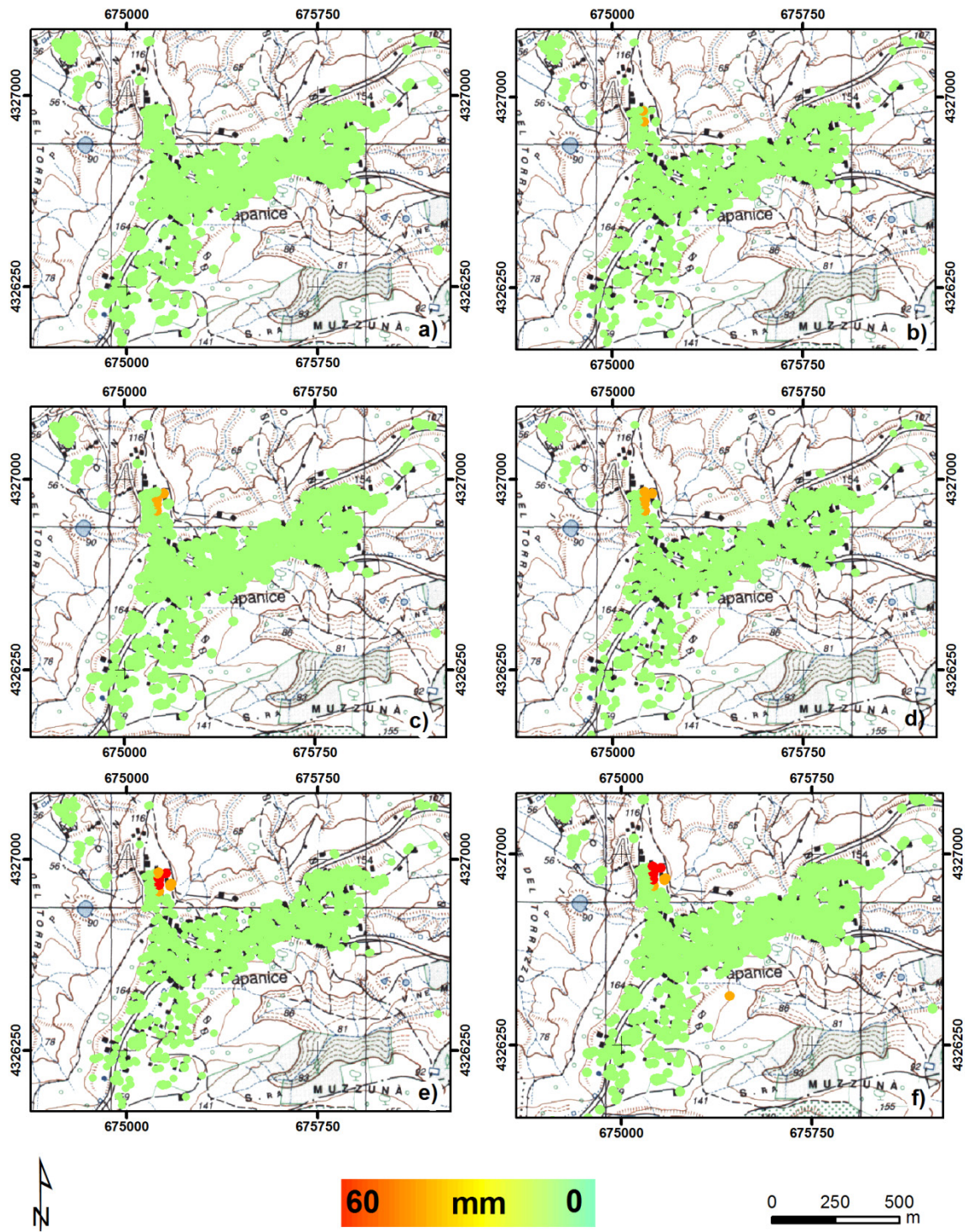
581 Moreover, the time series produced with the SBAS algorithm appears to be affected by higher noise (Figure 17), thus
582 showing less accurate measurements and proving to be not well suited for local deformations affecting, for example,
583 single buildings. In fact, the coarse resolution induced by the multilooking factors (5×5 for azimuth and range,
584 respectively, for the Papanice analysis) of SBAS algorithm led to an underestimation of the real velocities of
585 displacement. For this reason, the comparison between SAR and piezometric data has been carried out exclusively on
586 the CPT-TSC time series. With this method, more reliable velocities of the displacement have been obtained. Such
587 reliability is due to the comparison with rainfalls and piezometric data, and actually the activation of the displacement
588 begins when the rapid rise of the groundwater level occurs.

589 However, both SBAS and CPT-TSC were able to detect the area affected by displacements, as seen by the high
590 concentration of points located in the neighborhood of the slope (Figure 16 and 18). In Figures 24 and 25, the
591 displacement evolution of whole hamlet for pre- and post-failure activity, according to CPT-TSC results, are shown,
592 highlighting the progress of the deformation only in the Pironte neighborhood. This cluster falls within the main scarp,
593 and, as also displayed in the pre-failure phase, in the NW part of the landslide. In addition to the pre-failure movements
594 within the 2013-2014 time-span, there is also a clear evidence of an activation of movements in the opposite sector of
595 the landslide. In the SE part of it, clusters of at least 15 targets, showing average displacement rates of 5 mm/yr, have
596 been equally identified by the two techniques, and in both cases the maximum value of 8.3 mm/yr was measured, on a
597 target located in the backyard of a woodshed next to the slope. Hence, SAR analyses, even with different algorithms,
598 highlights a new sector of the landslide previously considered as stable, and, after the triggering phase, involved in the
599 instability. This remarkable result points out the critical role of such methods for predictive purposes. In fact, as it has
600 been possible to forecast the 2012 landslide in the 2008-2010 time-span, the same can be done in this second time

601 interval, hence considering this new area activation as a sign of a potential enlargement of the movement, thus
 602 involving new buildings and new areas. The integration of PSI methods with conventional devices and geotechnical
 603 analyses assumes, likewise, a paramount importance in the landslide analysis. The comparison between time series of
 604 displacement and piezometric monitoring showed the relationship of such phenomena with rainfalls and with
 605 oscillations of the water table level, clearly pointing out and confirming the role of groundwater for the slow-moving
 606 landslide triggering, as also proved during the slope stability test.
 607



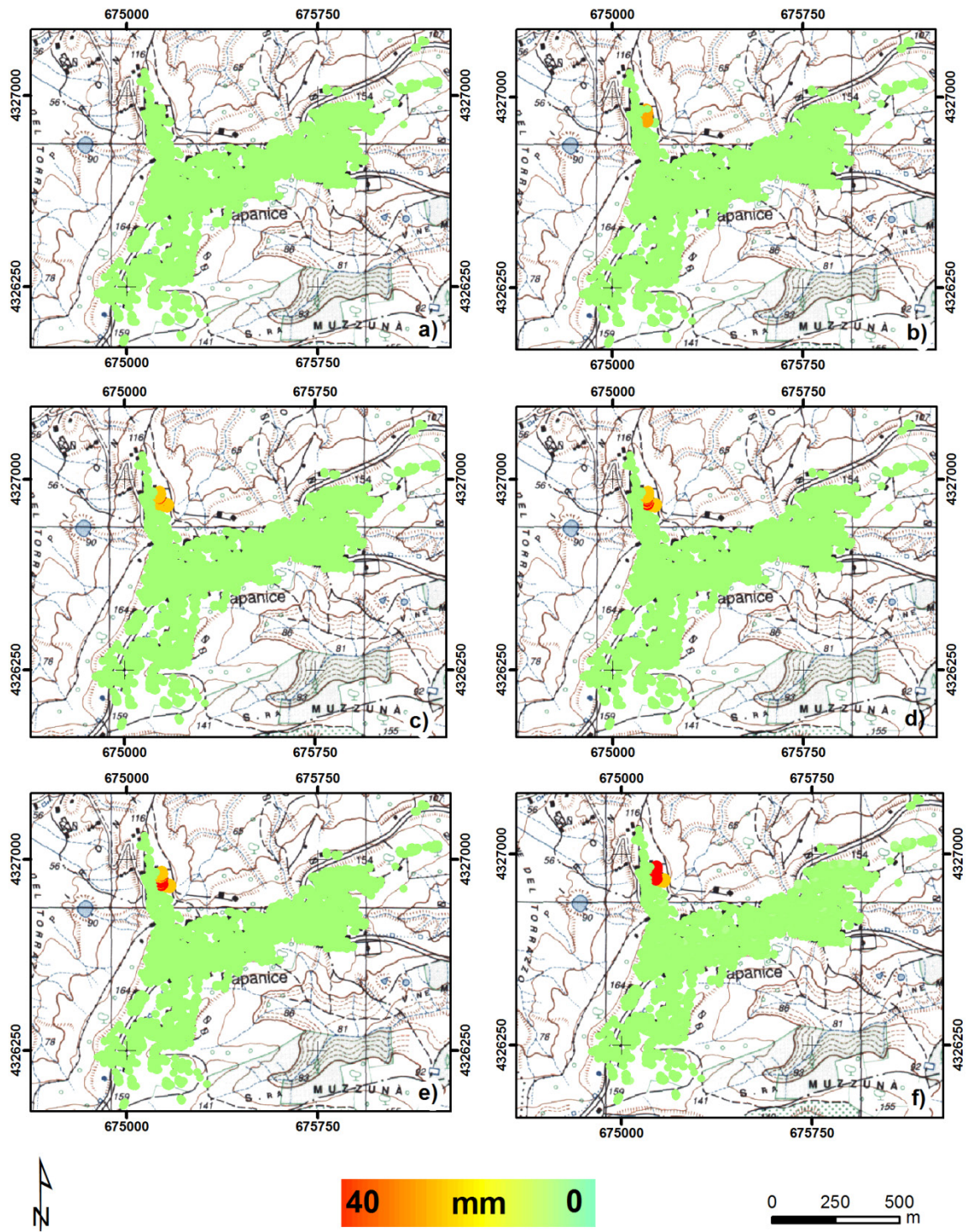
608
 609 **Figure 23** - Time series of displacement of the whole time-span monitored. The blue column highlights the time-span
 610 not covered by TerraSAR-X imagery. The red arrow shows the date of the slope failure (23th February 2012).



611

612 **Figure 24** – Pre-failure displacement evolution in Papanice. a) April 27, 2008; b) December 3, 2008; c) February 18,
 613 2009; d) June 30, 2009; e) January 3, 2010; f) June 28, 2010.

614



615

616 **Figure 25** – Displacement evolution in Papanice. a) October 9, 2013; b) February 18, 2014; c) June 30, 2014; d) August
 617 2, 2014; e) August 24, 2014; f) October 18, 2014.

618

619 9. Conclusion

620 This paper demonstrated the reliability of two Persistent Scatterers Interferometry (PSI) techniques for the
621 comprehension of gravitational phenomena such as slow-moving landslides, especially when coupled with conventional
622 methods. In this case, due to the presence of two different stacks, acquired during two separate time spans (2008–2010
623 and 2013–2014) it has been possible to follow the evolution of a slow-moving landslide case study, located in Crotona
624 municipality, in the hamlet of Papanice. Here, on February 23, 2012, after abundant precipitations (185 mm in 3 days,
625 ca. 28% of the average annual precipitation) a reactivation of a landslide already depicted in the Hydro-
626 Geomorphological Setting Plan (2006) by the Calabria Basin Authority occurred, causing damage to buildings and
627 utility lines. The precursor stages of the slope failure (2008–2010) were observed by means of PSI. Processing of the
628 second, post-failure, period of analysis (2013–2014) confirmed with two different approaches the state of activity
629 previously recognized on the NW sector of the landslide (characterized by average displacement rates along the Line of
630 Sight of -40 mm/yr), and detected the activation of a sector not considered before as unstable, with an average velocity
631 of -6 mm/yr along the LOS. The comparison between the Small Baseline Subset Approach (SBAS) and Coherent Pixel
632 Technique (CPT) with the Temporal Sublook Spectral Coherence pixel selection approach (TSC) highlighted their
633 different behavior on local scale studies, pointing out the better suitability of CPT-TSC in such contexts.

634 The slope stability analysis, finally, showed the supporting role of PSI techniques for geotechnical analyses. In this
635 case, the piezometric surface used as input for the test has been selected according to the comparison between the time
636 series and the groundwater monitoring, where an activation of the displacement has been recognized in occurrence of a
637 rapid rise of the water, reaching very shallow depths. Therefore, the integration between remote sensing and
638 conventional geological methods can represent a significant tool for intervention works planning, providing the right
639 indication on how and where to operate in order to reduce the risk and to increase the safety factor of the area. In
640 conclusion, we demonstrated the reliability of the PSI techniques for geological interpretation of a slow-moving
641 landslide, and how valid they are when coupled with geological and geomorphological field activities. These tools can
642 be considered a very useful instrument supporting urban planning or landslide hazard assessment, on behalf of public
643 administration.

644 Acknowledgments

645 TerraSAR-X data have been provided by the German Aerospace Center (DLR) through the GEO1589 and the
646 GEO2641 proposals. Authors would like to thank the department of GeoRisks and Civil Security (DLR) for the access
647 to SARscape. Thanks are also due to ARPACAL (Regional Agency for Environmental Protection of Calabria Region)
648 for providing rainfall and geological data. Thanks are also due anonymous reviewers for improving the quality of the

649 text. This work has been financed by Federico II University funds (project manager: D. Calcaterra) and by the Spanish
650 Science, Research and Innovation Plan (Ministerio de Economía y Competitividad) with Project Code TIN2014-55413-
651 C2-1-P.
652

653 **References**

- 654 Arnaud, A., Adam, N., Hanssen, R., Inglada, J., Duro, J., Closa, J., Eineder, M., 2003. ASAR ERS interferometric
655 phase continuity. International Geoscience and Remote Sensing Symposium, 21-25 July 2003, Toulouse (France),
656 (CDROM).
- 657 Bamler, R., Hartl, P., 1998. Synthetic aperture radar interferometry. *Inverse Problems* 14 (4), R1-R54. 10.1088/0266-
658 5611/14/4/001.
- 659 Bandini, A., Berry, P., Boldini, D., 2015. Tunnelling-induced landslides: The Val di Sambro tunnel case study.
660 *Engineering Geology* 196, 71–87, doi: 10.1016/j.enggeo.2015.07.001
- 661 Bardi, F., Frodella, W., Ciampalini, A., Bianchini, S., Del Ventisette, C., Gigli, G., Fanti, R., Moretti, S., Basile, G.,
662 Casagli, N., 2014. Integration between ground based and satellite SAR data in landslide mapping: The San Fratello case
663 study. *Geomorphology* 223, 45–60. 10.1016/j.geomorph.2014.06.025.
- 664 Beauducel, F., Briole, P., Froger, J., 2000. Volcano-wide fringes in ERS synthetic aperture radar interferograms of Etna
665 (1992-1998): Deformation or tropospheric effect? *Journal of Geophysical Research: Solid Earth* 105, B7, 16 391–16
666 402.
- 667 Berardino, P., Fornaro, G., Lanari, R., Sansosti, E., 2002. A new algorithm for surface deformation monitoring based on
668 small baseline differential SAR interferograms. *IEEE Trans. Geosci. Remote Sensing* 40 (11), 2375–2383.
669 10.1109/TGRS.2002.803792.
- 670 Bianchini, S., Ciampalini, A., Raspini, F., Bardi, F., Di Traglia, F., Moretti, S., Casagli, N., 2015. Multi-Temporal
671 Evaluation of Landslide Movements and Impacts on Buildings in San Fratello (Italy) By Means of C-Band and X-Band
672 PSI Data. *Pure appl. geophys.* 172 (11), 3043–3065. 10.1007/s00024-014-0839-2.
- 673 Blanco-Sanchez, P., Mallorquí, J.J., Duque, S., Monells, D., 2008. The Coherent Pixels Technique (CPT): An
674 Advanced DInSAR Technique for Nonlinear Deformation Monitoring. *Pure appl. geophys.* 165 (6), 1167–1193.
675 10.1007/s00024-008-0352-6.
- 676 Bonardi, G., Colonna, V., Dietrich, D., Giunta, G., Liguori, V., Lorenzoni, S., Paglionico, A., Perrone, V., Piccarreta,
677 G., Russo, M., Scandone, P., Zanettin Lorenzoni, A., Zuppeta, A., 1976. L'Arco calabro-peloritano, Carta Geologica
678 1:500.000, Società Geologica Italiana, 68° Congresso.
- 679 Bonì, R., Pilla, G., Meisina, C., 2016. Methodology for Detection and Interpretation of Ground Motion Areas with the
680 A-DInSAR Time Series Analysis. *Remote Sensing*, 8(8), 686.
- 681 Bozzano, F., Martino, S., Naso, G., Prestininzi, A., Romeo, R. W., Mugnozza, G. S., 2004. The large Salcito landslide
682 triggered by the 2002 Molise, Italy, earthquake. *Earthq. Spec.* 20(S1), S95-S105.

683 Brunetti, M., Maugeri, M., Monti, F., Nanni, T., 2004. Changes in daily precipitation frequency and distribution in Italy
 684 over the last 120 years. *Journal of Geophysical Research: Atmospheres*, 109(D5).
 685 Calabria Regional Basin Authority, 2006. Hydraulic-geological Setting Plan of the Calabria Region.
 686 Calcaterra, D., Di Martire, D., Ramondini, M., Calò, F., Parise, M., 2008. Geotechnical analysis of a complex slope
 687 movement in sedimentary successions of the southern Apennines (Molise, Italy), in: Chen, Z. (Ed.), *Landslides and
 688 engineered slopes. From the past to the future : proceedings of the Tenth International Symposium on Landslides and
 689 Engineered Slopes*, 30 June-4 July, 2008, Xi'an, China / editors, Zuyu Chen ... [et al.]. CRC Press, Boca Raton, pp.
 690 299–305.
 691 Calò, F., Calcaterra, D., Iodice, A., Parise, M., Ramondini, M., 2012. Assessing the activity of a large landslide in
 692 southern Italy by ground-monitoring and SAR interferometric techniques. *International Journal of Remote Sensing* 33
 693 (11), 3512–3530. 10.1080/01431161.2011.630331.
 694 Cascini, L., Fornaro, G., Peduto, D., 2010. Advanced low- and full-resolution DInSAR map generation for slow-moving
 695 landslide analysis at different scales. *Engineering Geology* 112 (1-4), 29–42. 10.1016/j.enggeo.2010.01.003.
 696 Centolanza, G., 2015. Quality evaluation of DInSAR results from the phase statistical analysis. PhD Thesis, 2015,
 697 <http://hdl.handle.net/10803/321363>
 698 Chaussard, E., Bürgmann, R., Shirzaei, M., Fielding, E. J., Baker, B., 2014. Predictability of hydraulic head changes
 699 and characterization of aquifer-system and fault properties from InSAR-derived ground deformation. *Journal of
 700 Geophysical Research: Solid Earth* 119(8), 6572-6590.
 701 Colesanti, C., Wasowski, J., 2006. Investigating landslides with space-borne Synthetic Aperture Radar (SAR)
 702 interferometry. *Engineering Geology* 88 (3-4), 173–199. 10.1016/j.enggeo.2006.09.013.
 703 158
 704 Confuorto P., Di Martire D., Ramondini M., Calcaterra D., 2014. Differential SAR interferometry for slow-
 705 moving landslide monitoring in Crotona Province (Italy). *Proceedings of ‘the Analysis and Management of
 706 Changing Risks for Natural Hazards conference’*, Padua, 18-19 November.
 707 Confuorto, P., Plank, S., Di Martire, D., Ramondini, M., Thuro, K., Calcaterra, D., 2015. Slow-Moving landslide
 708 monitoring with Multi-Temporal TerraSAR-X data by means of DInSAR tech-niques in Crotona province (Southern
 709 Italy). In *Proceedings of FRINGE’15: Advances in the Science and Applications of SAR Interferometry and Sentinel-1
 710 InSAR Workshop*, Frascati, Italy, 23-27 March 2015, Ouwehand L., Ed., ESA Publication SP-731.
 711 Cruden, D.M., Varnes, D.J., 1996. Landslide types and process. In *Landslides: Investigation and Mitigation*; Turner,
 712 A.K., Schuster, R.J. Eds. Publisher: Transportation Research Board, National Research Council, National Academy
 713 Press, Washington, DC, 1996, pp. 36–75.

714 D'Elia, B., Picarelli, L., Leroueil, S., Vaunat, J., 1998 Geotechnical characterisation of slope movements in structur-ally
715 complex clay soils and stiff jointed clays. *Rivista Italiana di Geotecnica* 32(3), 5-47.

716 Di Maio, C., Vassallo, R., Vallario, M., Pascale, S., Sdao, F., 2010. Structure and kinematics of a landslide in a com-
717 plex clayey formation of the Italian Southern Apennines. *Engineering Geology* 116(3), 311-322.

718 Di Martire, D., Rosa, M. de, Pesce, V., Santangelo, M.A., Calcaterra, D., 2012. Landslide hazard and land management
719 in high-density urban areas of Campania region, Italy. *Nat. Hazards Earth Syst. Sci.* 12 (4), 905–926. 10.5194/nhess-12-
720 905-2012.

721 Di Martire, D., Novellino, A., Ramondini, M., Calcaterra, D., 2016a. A-Differential Synthetic Aperture Radar
722 Interferometry analysis of a Deep Seated Gravitational Slope Deformation occurring at Bisaccia (Italy). *Science of the*
723 *Total Environment* 550, 556–573.

724 Di Martire, D., Ascione, A., Calcaterra, D., Pappalardo, G., Mazzoli, S., 2016b. Quaternary deformation in SE Sicily:
725 Insights into the life and cycles of forebulge fault systems. *Lithosphere* 7(5), 519-534.

726 Doin, M. P., Lasserre, C. Peltzer, G. Cavaliè, O., Doubre, C., 2009. Corrections of stratified tropospheric delays in SAR
727 interferometry: Validation with global atmospheric models. *Journal of Applied Geophysics* 69, 1, 35–50.

728 Duro, J., Closa, J., Biescas, E., Crosetto, M., Arnaud, A., 2005. High Resolution Differential Interferometry using time
729 series of ERS and ENVISAT SAR data. *Proc. Of the 6th. Geomatic Week Conference*, February 2005, Barcelona,
730 Spain (CDROM).

731 Esu, F., 1977. Behaviour of slopes in structurally complex formations. *Proceedings of the International Symposium on*
732 *the geotechnics of Structurally Complex Formations*, Capri, Italy, 1977, 292–304.

733 Ferretti A., Prati C., Rocca F., 2000. Nonlinear subsidence rate estimation using permanent scatterers in differential
734 SAR interferometry. *IEEE Transactions on Geoscience and Remote Sensing* 38 (5), 2202-2212.

735 Ferretti, A., Prati, C., Rocca, F., 2001. Permanent scatterers in SAR interferometry. *IEEE Trans. Geosci. Remote*
736 *Sensing* 39 (1), 8–20. 10.1109/36.898661.

737 Ferretti, A., Tamburini, A., Novali, F., Fumagalli, A., Falorni, G., Rucci, A., 2011a. Impact of high resolution radar
738 imagery on reservoir monitoring. *Energy Procedia* 4, 3465–3471.

739 Ferretti, A., Fumagalli, A., Novali, F., Prati, C., Rocca, F., Rucci, A., 2011b. A New Algorithm for Processing
740 Interferometric Data-Stacks: SqueeSAR. *IEEE Trans. Geosci. Remote Sensing* 49 (9), 3460–3470.
741 10.1109/TGRS.2011.2124465.

742 Franceschetti, G., Lanari, R., 1999. *Synthetic aperture radar processing*. CRC press, Boca Raton, FL, 1999.

743 Gabriel, A.K., Goldstein, R.M., Zebker, H.A., 1989. Mapping small elevation changes over large areas: Differential
744 radar interferometry. *J. Geophys. Res.* 94 (B7), 9183. 10.1029/JB094iB07p09183.

745 Gattinoni, P., Scesi, L., Arieni, L., Canavesi, M., 2012. The February 2010 large landslide at Maierato, Vibo Valentia,
 746 Southern Italy. *Landslides* 9(2), 255–261.

747 Guzzetti, F., Mondini, A.C., Cardinali, M., Fiorucci, F., Santangelo, M., Chang, K.-T., 2012. Landslide inventory maps:
 748 New tools for an old problem. *Earth-Science Reviews* 112 (1-2), 42–66. 10.1016/j.earscirev.2012.02.001.

749 Hanssen, R. F., 2001. *Radar interferometry: data interpretation and error analysis*. Dordrecht, The Netherlands: Kluwer,
 750 2001.

751 Herrera, G., Gutiérrez, F., García-Davalillo, J.C., Guerrero, J., Notti, D., Galve, J.P., Fernández-Merodo, J.A.,
 752 Cooksley, G., 2013. Multi-sensor advanced DInSAR monitoring of very slow landslides: The Tena Valley case study
 753 (Central Spanish Pyrenees). *Remote Sensing of Environment* 128, 31–43. 10.1016/j.rse.2012.09.020.

754 Hooper, A., H. Zebker, P. Segall, and B. Kampes, 2004. A new method for measuring deformation on volcanoes and
 755 other natural terrains using InSAR persistent scatterers, *Geophysical Research Letters*, 31(23), 5,
 756 doi:10.1029/2004GL021737, 2004.

757 Hooper, A., 2008. A multi-temporal InSAR method incorporating both persistent scatterer and small baseline
 758 approaches. *Geophys. Res. Lett.* 35 (16). 10.1029/2008GL034654.

759 Iglesias, R., Mallorqui, J. J., López-Dekker, P., 2014a. DInSAR Pixel Selection Based on Sublook Spectral Correlation
 760 Along Time. *IEEE Transactions on Geoscience and Remote Sensing* 52, 7, 3788–3799.

761 Iglesias, R., Fabregas, X., Aguasca, A., Mallorqui, J. J., López-Martínez, C., Gili, J. A., Corominas J., 2014b.
 762 Atmospheric Phase Screen Compensation in Ground- Based SAR With a Multiple-Regression Model Over
 763 Mountainous Regions. *IEEE Transactions on Geoscience and Remote Sensing* 52, 5, 2436– 2449.

764 Iglesias, R., Mallorqui, J. J., Monells, D., López-Martínez, C., Fabregas, X., Aguasca, A., Gill J. A., Corominas, J.,
 765 2015. PSI Deformation Map Retrieval by Means of Temporal Sublook Coherence on Reduced Sets of SAR Images.
 766 *Remote Sens.* 7(1), 530–563.

767 Janbu, N., 1954. Application of composite slip surfaces for stability analysis. In *Proceedings of European Conf. on*
 768 *Stability of Earth Slopes*, Stockholm, Sweden, 1954 (Vol. 3, 43-49).

769 Jolivet, R., Grandin, R., Lasserre, C., Doin, M.-P., Peltzer, G., 2011. Systematic In-SAR tropospheric phase delay
 770 corrections from global meteorological reanalysis data. *Geophysical Research Letters* 38, 17, 1–6.

771 Kropatsch, W.G., Strobl, D., 1990. The generation of SAR layover and shadow maps from digital elevation models.
 772 *IEEE Trans. Geosci. Remote Sensing* 28 (1), 98–107. 10.1109/36.45752.

773 Lagios, E., Sakkas, V., Novali, F., Bellotti, F., Ferretti, A., Vlachou, K., Dietrich, V., 2013. SqueeSAR™ and GPS
 774 ground deformation monitoring of Santorini Volcano (1992–2012): Tectonic implications. *Tectonophysics* 594, 38–59.

775 Lanari, R., Mora, O., Manunta, M., Mallorqui, J.J., Berardino, P., Sansosti, E., 2004. A small baseline approach for
 776 investigating deformations on full resolution Differential SAR Interferograms. *IEEE Transactions on Geoscience and*
 777 *Remote Sensing* 42, 1377–1386.

778 Manconi, A., Casu, F., Ardizzone, F., Bonano, M., Cardinali, M., De Luca, C., Gueguen, E., Marchesini, I., Parise, M.,
 779 Vennari, C., Lanari, R., Guzzetti, F., 2014. Brief Communication: Rapid mapping of landslide events: the 3 December
 780 2013 Montescaglioso landslide, Italy. *Nat. Hazards Earth Syst. Sci.* 14, 1835–1841.

781 Massari, F., Rio, D., Sgavetti, M., Prosser, G., D'Alessandro, A., Asioli, A., Capraro, L., Fornaciari, E., Tateo, F., 2002.
 782 Interplay between tectonics and glacio-eustasy: Pleistocene succession of the Crotone basin, Calabria (southern Italy).
 783 *Geological Society of America Bulletin* 114 (10), 1183–1209. 10.1130/0016-7606(2002)114<1183:IBTAGE>2.0.CO;2.

784 Massonnet, D., Rabaute, T., 1993. Radar interferometry: limits and potential. *IEEE Trans. Geosci. Remote Sensing* 31
 785 (2), 455–464. 10.1109/36.214922.

786 Meulenkamp, J.E., Hilgen, F., Voogt, E., 1986. Late Cenozoic sedimentary tectonic history of the Calabrian Arc.
 787 *Giornale di Geologia* 48(1–2), 345–359.

788 Modoni, G., Darini, G., Spacagna, R.L., Saroli, M., Russo, G., Croce, P., 2013. Spatial analysis of land subsidence
 789 induced by groundwater withdrawal. *Engineering Geology* 167, 59–71, doi: 10.1016/j.enggeo.2013.10.014

790 Mohr, O., 1914. *Treatises on mechanic-engineering* (2nd ed). 1914. Ernst, Berlin. (In German)

791 Mora, O., Mallorqui, J.J., Broquetas, A., 2003. Linear and nonlinear terrain deformation maps from a reduced set of
 792 interferometric sar images. *IEEE Trans. Geosci. Remote Sensing* 41 (10), 2243–2253. 10.1109/TGRS.2003.814657.

793 Notti, D., Davalillo, J.C., Herrera, G., Mora, O., 2010. Assessment of the performance of X-band satellite radar data for
 794 landslide mapping and monitoring: Upper Tena Valley case study. *Nat. Hazards Earth Syst. Sci.* 10 (9), 1865–1875.
 795 10.5194/nhess-10-1865-2010.

796 Notti, D., Herrera, G., Bianchini, S., Meisina, C., García-Davalillo, J.C., Zucca, F., 2014. A methodology for im-
 797 proving landslide PSI data analysis. In: *J. Remote Sens.* 35(6), 2186–2214.

798 Novellino, A., Cigna, F., Sowter, A., Syafiudin, M.F., Di Martire, D., Ramondini, M., Calcaterra, D., 2015. Intermittent
 799 small baseline subset (ISBAS) InSAR analysis to monitor landslides in Costa della Gaveta, Southern Italy. *IEEE*
 800 *International Geoscience and Remote Sensing Symposium, IGARSS 2015; Milan; Italy; 26 - 31 July 2015, Volume*
 801 *2015-November*, Article number 7326584, Pages 3536-3539.

802 Paradella, W.R., Ferretti, A., Mura, J.C., Colombo, D., Gama, F.F., Tamburini, A., Santos, A.R., Novali, F., Galo, M.,
 803 Camargo, P.O., Silva, A.Q., Silva, G.G., Silva, A., Gomes, L.L., 2015. Mapping surface deformation in open pit iron
 804 mines of Carajás Province (Amazon Region) using an integrated SAR analysis. *Engineering Geology* 193, 61–78.

805 Plank, S., Singer, J., Thuro, K., 2013. Assessment of number and distribution of persistent scatterers prior to radar
806 acquisition using open access land cover and topographical data. *ISPRS Journal of Photogrammetry and Remote*
807 *Sensing* 85, 132–147. 10.1016/j.isprsjprs.2013.09.001.

808 Prati, C., A. Ferretti, Perissin, D., 2010. Recent advances on surface ground deformation measurement by means of
809 repeated space-borne SAR observations. *J. Geodyn.* 49, 161–170, doi:10.1016/j.jog.2009.10.011.

810 Raspini, F., Ciampalini, A., Del Conte, S., Lombardi, L., Nocentini, M., Gigli, G., Ferretto, A., Casagli, N., 2015.
811 Exploitation of Amplitude and Phase of Satellite SAR Images for Landslide Mapping: The Case of Montescaglioso
812 (South Italy). *Remote Sensing* 7(11), 14576-14596.

813 Regional agency for the environmental protection of Calabria Region (ARPACAL), 2013. Installation of a real time
814 monitoring system of the Pironte and of the Via Oceania Primary School landslides, in Papanice, Crotona. (In Italian).

815 Remy, D., Bonvalot, S., Briole, P., Murakami, M., 2003. Accurate measurements of tropospheric effects in volcanic
816 areas from SAR interferometry data: application to Sakurajima volcano (Japan). *Earth and Planetary Science Letters*
817 213, 3–4, 299 – 310.

818 Research Institute for Geo-Hydrological Protection (IRPI), 2015. Periodic report on landslides and floods hazard for the
819 Italian population 2015. (In Italian).

820 Roda, C., 1964. Facies and distribution of Neogenic sediments in the Crotona Basin. *Geologica Romana* 3, 319–366 (In
821 Italian).

822 Scaioni, M., Longoni, L., Melillo, V., Papini, M., 2014. Remote Sensing for Landslide Investigations: An Overview of
823 Recent Achievements and Perspectives. *Remote Sens.* 6, 9600-9652.

824 Schneider, U., Fuchs, T., Meyer-Christoffer, A., Rudolf, B., 2008. Global precipitation analysis products of the GPCC.
825 Global Precipitation Climatology Centre (GPCC), DWD, Internet Publikation, 112.

826 Schuster, R. L., Fleming, R. W., 1986. Economic losses and fatalities due to landslides. *Bulletin of the Association of*
827 *Engineering Geologists* 23(1), 11-28.

828 Sowter, A., Bateson, L., Strange, P., Ambrose, K., Syafiudin, M.F., 2013. DInSAR estimation of land motion using
829 intermittent coherence with application to the South Derbyshire and Leicestershire coalfields. *Remote Sensing Letters*
830 4, 979-987.

831 Tofani, V., Segoni, S., Agostini, A., Catani, F., Casagli, N., 2013. Technical Note: Use of remote sensing for landslide
832 studies in Europe. *Nat. Hazards Earth Syst. Sci.* 13 (2), 299–309. 10.5194/nhess-13-299-2013.

833 Valipour, M., Sefidkouhi, M. A. G., Eslamian, S., 2015. Surface irrigation simulation models: a review. *International*
834 *Journal of Hydrology Science and Technology* 5(1), 51-70.

835 Valipour, M., 2016. Optimization of neural networks for precipitation analysis in a humid region to detect drought and
836 wet year alarms. *Meteorological Applications* 23(1), 91-100.

837 Van Dijk, J.P., 1990. Sequence stratigraphy, kinematics and dynamic geohistory of the Croton Basin (Calabria Arc,
838 Central Mediterranean): an integrated approach. *Memorie della Società Geologica Italiana* 44, 259–285.

839 Van Dijk, J.P., 1991. Basin dynamics and sequence stratigraphy in the Calabrian Arc (Central Mediterranean): rec-ords
840 and pathways of the Croton Basin. *Geologie en Mijnbouw* 70, 187–201.

841 Van Dijk, J.P., Okkes, M., 1990. The analysis of shear zones in Calabria: Implications for the geodynamics of the
842 Central Mediterranean. *Ric. Sci., Suppl.* 68, 24–27.

843 Van Dijk, J., Okkes, M., 1991. Neogene tectonostratigraphy and kinematics of Calabrian basins; Implications for the
844 geodynamics of the Central Mediterranean. *Tectonophysics* 196 (1-2), 23–60. 10.1016/0040-1951(91)90288-4.

845 Vennari, C., Gariano, S.L., Antronico, L., Brunetti, M.T., Iovine, G., Peruccacci, S., Terranova, O., Guzzetti, F., 2014.
846 Rainfall thresholds for shallow landslide occurrence in Calabria, southern Italy. *Nat. Hazards Earth Syst. Sci.* 14 (2),
847 317–330. 10.5194/nhess-14-317-2014.

848 Wasowski, J., Bovenga, F., 2014. Investigating landslides and unstable slopes with satellite Multi Temporal Inter-
849 ferometry: Current issues and future perspectives. *Eng. Geol.* 174, 103-138.

850 Webley, P. W., Bingley, R. M., Dodson, A. H., Wadge, G., Waugh, S. J., James, I. N., 2002. Atmospheric water vapour
851 correction to InSAR surface motion measurements on mountains: results from a dense GPS network on Mount Etna.
852 *Physics and Chemistry of the Earth* 27, 4–5, 363–370.

853 Wegmuller, U., Werner, C., Strozzi, T., 1998. SAR interferometric and differential interferometric processing chain. In
854 *Proceedings of IGARSS'98, Seattle, WA, July 6–10, 1998*, 1106–1108. vol.2.

855 Werner, C., Wegmüller, U., Strozzi, T., Wiesmann, A., 2003. Interferometric point target analysis for deformation
856 mapping. *Proceedings of IGARSS*, 21–25 July 2003, Toulouse (France), CDROM.

857 Williams, S., Bock, Y., Fang, P., 1998. Integrated satellite interferometry: Tropospheric noise, GPS estimates and
858 implications for interferometric synthetic aperture radar products. *Journal of Geophysical Research: Solid Earth* 103,
859 B11, 27 051–27 067.

860 WP/WLI (International Geotechnical Societies' UNESCO Working Party on World Landslide Inventory) 1993. A
861 suggested method for describing the activity of a landslide, *Bulletin International Association of Engineering Geology*,
862 47: 53-57.

863 <http://www.geostru.com/EN/Slope-stability-analysis.aspx> (accessed on 20 September 2015).

864 www.sarmap.ch (accessed on 12 October 2014).

865 Zecchin, M., Caffau, M., Civile, D., Critelli, S., Di Stefano, A., Maniscalco, R., Muto, F., Sturiale, G., Roda, C., 2012.
866 The Plio-Pleistocene evolution of the Crotona Basin (southern Italy): Interplay between sedimentation, tectonics and
867 eustasy in the frame of Calabrian Arc migration. *Earth-Science Reviews* 115 (4), 273–303.
868 10.1016/j.earscirev.2012.10.005.

869 **LIST OF FIGURE CAPTIONS**

870 **Figure 1** - Map of the landslide events with “victims” in the time span 1964-2013, with the spread of the Structurally
871 Complex Formations (SCFs) in the whole Italian territory (modified from IRPI, 2015). In the red box, Calabria region.

872 **Figure 2** - a) Geological sketch map of Crotona province: 5 – Meta-limestones, phyllites (Devonian age); 6 – Granites
873 (Permian-Carboniferous age); 37 - Varicolored clays (Tortonian age); 38 - Clays and marls, evaporitic deposits (Lower
874 Pliocene-Tortonian age); 39 – Calcarenes, sands, clays and conglomerates (Lower Pleistocene – Middle Pleistocene
875 age); 40 – Alluvial deposits (Holocene – Upper Pleistocene). In blue bands, the two shear zones. Modified from
876 Bonardi et al., 1976 ; b) Geological sketch map of Papanice area: 1 - Recent Alluvial Deposits (Holocene), 2 -
877 Sant’Anna Synthem (Ionian), 3 - Cutro marly-clayey Formation (Piacentian – Calabrian) (SCF formation). In blue
878 square, Pironte district; c) Urban evolution of Papanice settlement during 1953-2014: green = urban area before 1955,
879 yellow= 1956-1982 expansion, red= 1983-2014 expansion (modified from ARPACAL, 2013). In blue square, Pironte
880 district.

881 **Figure 3** - Landslide inventory map of Papanice, modified from Calabria Regional Basin Authority, 2006. 1) Slide; 2)
882 Complex landslide; 3) Area affected by shallow slow deformation/movements; 4) Area affected by deep slow
883 deformation/movements; 5) Area affected by deep erosion. The blue square marks the area interested by the 2012
884 landslides (Pironte district).

885 **Figure 4** - Localization of the measurement stations of the Multi-hazard Functional Center of the ARPACAL and
886 rainfall amount for the period 21-23 February 2012.

887 **Figure 5.** a) Localization of Papanice rain gauge. In blue rectangle the area interested by the 2012 landslide events.
888 Daily (blue columns) and cumulative (red line and red numbers) rainfall values for: b) year 2012; c) February 2012; d)
889 19-25 February 2012.

890 **Figure 6** - Rainfall duration vs. cumulated event rainfall, conditions which resulted in shallow landslides in Calabria
891 (red dots), and related threshold with a 95% confidence level. Shaded areas show uncertainties associated with the
892 threshold. Blue dot = Papanice landslide. Modified from Vennari et al., 2014.

893 **Figure 7.** Field survey landslide inventory map of the Pironte district

894 **Figure 8.** a) Landslide main scarp (Modified from Confuorto et al., 2015); b) Detail of the SW landslide and monitoring
895 system installed after the 2012 main reactivation.

896 **Figure 9** - Geolithological section A-A'. The location of the section is shown in Figure 7. Keys to the Units are given in
897 the text. I1 is the inclinometer, S1 and S2 are the two boreholes along the section.

898 **Figure 10** - a) Measurements of the inclinometer I1; b) Comparison between piezometric data from piezometer P1 (blue
899 line) and daily rainfall at Papanice rain gauge (red).

900 **Figure 11** - R-Index computation for ascending (a) and descending (b) orbits. Red colors show the layover areas (R-
901 Index < 0), yellow areas show foreshortening ($0 < \text{R-Index} < 0.4$), green areas mark a good visibility ($\text{R-Index} \geq 0.4$).
902 Landslides are reported in purple line.

903 **Figure 12** - a) Displacement rate map obtained with the CPT-TSC algorithm for the time interval 2008-2010. In the
904 purple rectangle, a zoom-in of the area of interest (b). Landslides have been reported in brown-dashed line. The points
905 S-TSC and TSC1 have been selected for the time series analysis (Figure 13). Modified from Confuorto et al. (2015).

906 **Figure 13** – Time series of displacement of the points S-TSC (green) and TSC1 (red). Modified from Confuorto et al.
907 (2015).

908 **Figure 14** - a) Displacement rate map obtained with the PS (1st period of analysis) algorithm for the time interval 2008-
909 2009. In the purple rectangle, a zoom-in of the area of interest (b). Landslides have been reported in brown-dashed line.
910 The points S-PS and PS1 have been selected for the time series analysis (Figure 15). Modified from Confuorto et al.
911 (2015).

912 **Figure 15** - Time series of displacement of the points S-PS (green) and PS1 (red). Modified from Confuorto et al.
913 (2015).

914 **Figure 16** - a) Displacement rate map obtained with the SBAS method for the time interval 2013–2014. In the purple
915 rectangle, a zoom-in of the area of interest (b). Landslides have been reported in brown-dashed line. The points S-SBAS
916 and SBAS1 have been selected for the time series analysis (Figure 17).

917 **Figure 17**- Time series of displacement of the points S-SBAS (green) and SBAS1 (red).

918 **Figure 18** - a) Displacement rate map obtained with the CPT-TSC method for the time interval 2013–2014. In the
919 purple rectangle, a zoom in of the area of interest (b). Landslides have been reported in brown-dashed line. The point
920 TSC2 has been selected for the time series analysis (Figure 19).

921 **Figure 19** - Comparison between piezometric and rainfall data with time series obtained with the CPT-TSC algorithm.
922 On the top bar, the average trends of the TSC2 time series. The average LOS velocities are shown for the slowing and
923 accelerating trends. Dashed lines show the connection between piezometric level and acceleration and deceleration of
924 the ground movement. The blue shaded column is for the rainy period between November 11, 2013 and December 4,
925 2013, correspondent to a rapid rise of piezometric level.

926 **Figure 20** - Profiles of the slope of analysis: pre-event configuration (red line), post-event configuration (black line).
927 The location of the section is shown in Figure 8b.

928 **Figure 21** - Back-analysis simulation, where the three hypothetical slip surfaces are represented with red-dashed lines.
929 I1 is the inclinometer, S1 and S2 are the two boreholes along the section.

930 **Figure 22** - Stability analysis on the post-event profile. The slip surface identified is indicated in red-dashed line. The
931 vertical red lines represents the different slices drew following Jambu method. I1 is the inclinometer, S1 and S2 are the
932 two boreholes along the section.

933 **Figure 23** - Time series of displacement of the whole time-span monitored. The blue column highlights the time-span
934 not covered by TerraSAR-X imagery. The red arrow shows the date of the slope failure (23th February 2012).

935 **Figure 24** – Pre-failure displacement evolution in Papanice. a) April 27, 2008; b) December 3, 2008; c) February 18,
936 2009; d) June 30, 2009; e) January 3, 2010; f) June 28, 2010.

937 **Figure 25** – Displacement evolution in Papanice. a) October 9, 2013; b) February 18, 2014; c) June 30, 2014; d) August
938 2, 2014; e) August 24, 2014; f) October 18, 2014.